Article

Surface Structuring and Thin Film Coating through Additive Concept Using Laser Induced Plasma of Mg Alloy: A Comparison between the Presence and Absence of Transverse Magnetic Field (TMF)

Asadullah Dawood [1,*] , Shazia Bashir [1], Naveed Ahmed [2,*] , Asma Hayat [1], Abdullah Yahia AlFaify [3] , Syed Muhammad Abouzar Sarfraz [4], Shahab Ahmed Abbasi [5] and Ateekh Ur Rehman [3]

1 Centre for Advanced Studies in Physics (CASP), Government College University, Lahore 54000, Pakistan
2 Department of Industrial Engineering, College of Engineering and Architecture, Al Yamamah University, Riyadh 11512, Saudi Arabia
3 Industrial Engineering Department, College of Engineering, King Saud University, P.O. Box 800, Riyadh 11421, Saudi Arabia
4 Dipartimento Interateneo di Fisica, Università degli Studi di Bari Aldo Moro, I-70126 Bari, Italy
5 Department of Physics, King Abdullah Campus, University of Azad Jammu & Kashmir, Muzaffarabad 13100, Pakistan
* Correspondence: asaddawood@gmail.com (A.D.); n_ahmed@yu.edu.sa (N.A.); Tel.: +92-332-4234070 (A.D.); +92-336-4647741 (N.A.)

Abstract: In the present study, the influence of a 1.1 tesla Transverse Magnetic Field (TMF) on Laser-Induced Breakdown Spectroscopy (LIBS) of Mg-alloy plasma has been explored. The Mg plasma was produced using an Nd: YAG laser (1064 nm, 10 ns) at an intensity of 2 GW/cm^2. Inert gases of Ar, Ne, and He were filled as environmental gases at pressures ranging from 1 to 100 Torr. Optical emission spectra from laser-produced plasma were detected with the help of a spectrometer, and plasma parameters such as excitation temperature (T_{exc}) and electron number density (n_e) were evaluated. Enhancement in the Mg plasma's T_{exc} and n_e in the presence of TMF was noticed under all experimental conditions, including different ambient gases with varying pressures and time delays (0.42 μs–9.58 μs). Plasma confinement by applied TMF was analytically evaluated through thermal beta (β_t) values, which were <1 under all circumstances. The highest T_{exc} and n_e values (17,259 K and 11.5×10^{17} cm^{-3}) for Mg-alloy plasma were obtained with ambient Ar in TMF, while the lowest values (8793 K and 1.0×10^{17} cm^{-3}) were obtained in presence of He gas in the absence of TMF. SEM analysis was used to determine the surface structure of laser-ablated Mg alloy in the presence and absence of TMF. It revealed that the formation of cones, cavities, and non-uniform melting are characteristic features of ambient Ar, while spikes and cavities are prominent features in Ne gas environments. Conical spikes and dendrites are distinct features when ambient He is present. In comparison with the field-free condition, distinct and well-defined structures were observed in the presence of TMF. By controlling LPP parameters, the surface structuring of Mg alloy can be controlled. The optimization and enhancement of LPP parameters make it a highly useful tool for thin film deposition, coatings of multilayers, and ion implantation/doping.

Keywords: transverse magnetic field; excitation temperature; number density; ambient pressures; delay time; surface structuring

1. Introduction

Laser ablation is a well-established technique for material processing owing to its extensive variety of applications in the fields of pulsed-laser deposition of thin films, micro/nano structuring, material machining, plasma processing, and ion-implantation [1–8].

Laser-induced breakdown spectroscopy (LIBS) is a reliable and simple technique for elemental analysis as well as for evaluating the T_{exc} and n_e of laser produced plasma (LPP). The employment of an appropriate transverse magnetic field (TMF) to LPP can limit the free expansion of plasma species and result in a variety of physical processes, including magnetic confinement [9], Joule's heating effect [10], conversion of kinetic energy to plasma thermal energy [11], alteration in trajectories of charged species caused by Lorentz force [12], and variation in plasma instabilities [1]. All of these phenomena contribute to the enhancement of the T_{exc} and n_e of plasmas [1,13]. Magnetic field confinement of LPP has drawn significant attention from the LIBS research community over the past few years. The magnetically confined plasma increases the collisional ionization, resulting in strong enhancement of weaker or previously unobserved spectral lines of various elements, especially of trace elements in a material. In this way, magnetic fields have provided a very efficient method of increasing the Limit of Detection (LOD) in the LIBS technique.

Previously, several researchers have explored the enhancement of emission intensity, T_{exc}, and n_e in the presence of TMF. For example, Atiqa et al. [14] investigated the effect of TMF (0.5 T) on the emission spectra of graphite plasma as a function of laser fluence in ambient gas. The laser fluence was varied between 0.4 and 2.9 J.cm^{-2} in two environments of air and Ar at 150 and 760 torr, respectively. The introduction of TMF increased the spectral intensity, T_{exc}, and n_e at all fluences and environmental conditions. The plasma parameters' efficacy was attributed to the Joule's heating effect and magnetic confinement. Li et al. [15] employed spectral and temporal resolved emission spectroscopy to investigate the impact of TMF on the LPP of a Cu target. They determined the emission intensity, T_{exc}, and n_e of Cu LPP with and without TMF at various time delays. They observed a substantial increase in the spectral line intensity as well as T_{exc} and n_e in the presence of TMF as compared to the field-free condition. They found that this rise in all LPP parameters of Cu is attributable to an increase in the plasma's radiative recombination rate owing to magnetic confinement. Ye et al. [16] demonstrated that when TMF is applied to Cu film plasma, an increase in ablation depth during laser drilling was seen. They discovered that by applying a continuous magnetic field to LPP they could enhance the aspect ratio and ns-laser ablation speed, which is attributable to plasma magnetic confinement. Neogi et al. [9] investigated the impact of non-uniform TMF on the LPP of carbon under both vacuum and low ambient pressures. They evaluated spectral intensity, T_{exc}, and n_e under various temporal and ambient pressure conditions. They found that in the presence of a TMF, all LPP parameters are substantially increased across temporal variations as well as at various ambient pressures. They found that enhancements in all LPP parameters are caused by magnetic confinement, the J×B effect, Joule heating, and greater interparticle collisions caused by adiabatic compression. Abbasi et al. [17] demonstrated an increase in optical emission from a palladium (Pd) sample using magnetic field-aided LIBS. At low laser fluence (12.6 J/cm^2), a considerable boost in plasma emission was recorded for both neutral and singly ionized lines of Pd. Additionally, the LPP parameters T_{exc} and n_e were significantly elevated in the presence of the magnetic field. In another study of LPP, Waheed et al. [18] examined the impact of TMF on the LPP of ZrO_2. They discovered that although both emission intensity and T_{exc} rose with increasing laser fluence, the n_e of ZrO_2 plasma decreased with increasing laser fluence. They found that the emission intensity, T_{exc}, and n_e of ZrO_2 plasma are somewhat higher in the presence of a TMF than in the absence of a TMF at all fluences. Magnetic confinement and the Joule heating effect are responsible for this rise in plasma characteristics. Aguilera et al. [19] reported time-resolved measurements of the T_{exc} and n_e of steel LPPs in a variety of ambient circumstances, including air, Ar, and He. They discovered that He is responsible for LPP parameters degrading at a faster rate than those of other gases. Hussain et al. [20] investigated the effect of an applied magnetic field on LIBS emission at various air pressures and time delays using an aluminum sample. They observed significant improvement (primarily at low pressure and shorter delay times) for Al atomic lines due to the effect of the 0.5 T magnetic field, although signal enhancement of approximately two-fold was obtained for the Al (I) 396.1 nm spectral line at a higher

air pressure of 100 Pa and a delay time of 100 ns. They observed that signal improvement occurs as a result of magnetic confinement, which increases the rate of electron impact excitation and recombination processes. Additionally, they analyzed plasma properties such as electron temperature and electron number density, and observed a considerable rise with TMF when compared to the field-free condition. In our own recent work, we studied the micro/nanostructure of Mg alloy under Ar, Ne, and He gases. The formation of cones, craters, and cavities were found to be strongly dependent on the laser irradiance, magnetic field, and ambient environment.

Magnesium (Mg) alloys have recently acquired attention as a material of study in the field of biomedical physics thanks to their use in the replacing stents and orthopaedic implants, thereby challenging conventional paradigms related to corrosion-resistant metallic implants. An Mg alloy with the commercial designation AZ31 (Mg: 96%; Al: 3% and Zn: 1%) was selected as the target material due to its high biocompatibility and closeness to the human body. As this alloy is non-toxic, it may enhance bone cell adhesion and tissue growth on implants. In addition, it may facilitate the replacement of stents by modulating their corrosion resistance. Due to the exceptional biodegradability of this alloy there is no need for a second surgery after its implantation, as it gradually disappears as the surgical wounds heal. More intriguingly, the AZ31 implant has unique characteristics, such as its density (1.74–2 g/cm^3) and Young's modulus (41–45 GPa), which are quite comparable to the density and Young's modulus of human bones (1.8–2.1 g/cm^3 and 3–20 GPa, respectively). Due to the biocompatibility of AZ31, there is no stress shielding effect; all stress is passed to the bone-implant contact. As a consequence, Mg alloy hinders the formation of new bone and reduces the longevity of implants.

The current study investigates the impact of TMF on laser-induced Mg alloy plasma characteristics at various pressures of Ar, Ne, and He as well as at varied time delays and surface structuring correlations, with the plasma parameters established in order to enhance the alloy's use in biocompatible applications. Two permanent magnets were utilised to produce a 1.1 Tesla TMF. In the first set of experiments, the LIBS technique was used to investigate LPP of Mg under various ambient environments of Ar, Ne, and He at pressures ranging from 1 Torr to 100 Torr and a fixed optimized laser irradiance of 2.0 GW/cm^2. In the second set of experiments, the LPP parameters of Mg were investigated at various time delays ranging from 0.42 μs to 9.58 μs and a fixed optimized laser irradiance of 2.0 GW/cm^2. Two plasma characteristics, T_{exc} and n_e, were used to characterize the LPP of Mg. T_{exc} was measured using the Boltzmann Plot technique, while ne was evaluated using the Stark broadening method. After irradiation, surface features were grown and then investigated by SEM. We computed the plasma confinement parameters such as thermal β_t analytically in order to verify the validity of magnetic confinement in the presence of the 1.1 Tesla TMF

2. Experimentation

The experimental setup is schematically shown in Figure 1. The target material was an Mg alloy with the industrial name AZ31 (Mg: 96%; Al: 3% and Zn: 1%). It was purchased from Alpha Aesar (Ward Hill, Massachusetts, USA). For laser irradiation, circular samples of Mg alloy targets with 20 mm diameter and 10 mm thickness were cut. Samples were subjected to mechanical grinding and polishing, then ultrasonically cleaned for 20 min to remove any contamination prior to laser ablation.
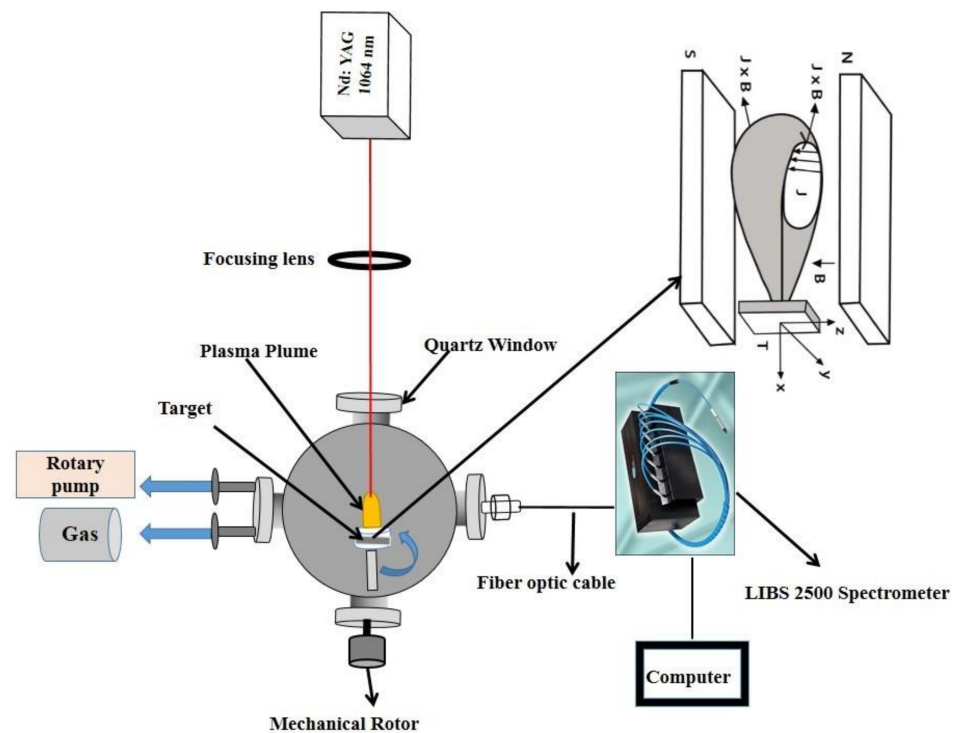
Figure 1. Schematic of the experimental setup for investigating the impact of magnetic fields on the laser-induced breakdown spectroscopy of Mg alloy plasma produced with an Nd: YAG laser.

Samples were placed on a revolving target holder within a vacuum chamber to provide a fresh surface for each laser shot in order to avoid crater formation due to deep drilling. Using a rotary pump, the chamber was evacuated to 10^{-3} Torr residual base pressure. Two 5 cm $\times$ 5 cm square-shaped permanent neodymium magnets were used to produce a 1.1 Tesla TMF. A Guess meter (GM07 HIRST, Magnetic Instruments Ltd. Falmouth, UK) was used to measure MF strength. To employ the TMF, magnets were placed at a distance of 3 cm in such a way that the magnetic lines of force passed perpendicular to the LPP. For LIBS analysis, a Q-Switched Nd: YAG (CRF200: Big Sky Laser Technologies, Quantel, France) laser system was used. Experiments were performed using a 1064 nm Nd: YAG laser with a pulse length of 10 ns and a repetition rate of 1–10 Hz. The laser beam irradiated the alloy sample in a direction orthogonal to the target surface after passing through the focusing lens of focal length 50 cm, producing the plasma. By keeping laser irradiance constant at 2.0 GW/cm^2, the nature of the ambient gas along with its pressure and delay time could be varied. The laser pulse energy was measured by a Joule meter.

Optical emissions from the LPP were captured by CCD camera through optical fiber and a collected lens of focal length 5 cm. The emission spectra were analyzed using the OOLIBS software (LIBS2500, Ocean Optics, Dunedin, Florida, USA, 200–980 nm, 2.1 ms). After creating a vacuum, the chamber was filled with inert gases (Ar, Ne, and He) at different pressures for various sets of experiments. Three sets of experiments were conducted.

i.   In the first set of experiments, Ar, Ne, and He were used as environmental gases. All background gases were supplied at 15 different pressures of 1, 2, 3, 4, 5, 10, 20, 30, 40, 50, 60, 70, 80, 90 and 100 Torr. In this set, the Mg alloy target was exposed to a single laser pulse of 150 mJ energy with an irradiance of 2.0 GW/cm^2 at 1.25 μs. Time delay and plasma emissions were captured in both the absence and presence of a TMF.

ii.   In the second set of experiments, the time delay was varied from 0.42 to 9.58 μs for cases both with and without magnetic field. For this set of experiments, all inert gases, again Ar, Ne, and He, were filled turn by turn in the chamber under a constant pressure of 5 Torr and at a constant irradiance of 2.0 GW/cm^2.

iii. In order to correlate the LPP parameters with the growth of surface structures, a third set of experiment was performed by exposing the Mg alloy target to 200 laser shots in different environmental conditions, including Ar, Ne, and He at 5 Torr pressure and irradiance 2.0 GW/cm^2, where the maximum LPP parameters are achieved. SEM analysis was performed in order to explore the surface structures of the laser-irradiated Mg alloy. For this purpose, a JEOL JSM 6490-A Scanning Electron Microscope (Tokyo, Japan) was used.

3. Results

3.1. Effect of Transverse Magnetic Field

Figure 2 illustrates the emission intensity of Mg (I) lines in the presence of the TMF (solid) and in the field-free case (dotted curve) across the spectral range from 370 nm to 520 nm at an irradiance of 2.0 GW/cm^2 under Ar, Ne, and He at a pressure of 5 Torr. Four strong Mg spectral lines with wavelengths of 382.93 nm, 389.12 nm, 470.30 nm, and 517.27 nm are selected for LPP parameters evaluation.
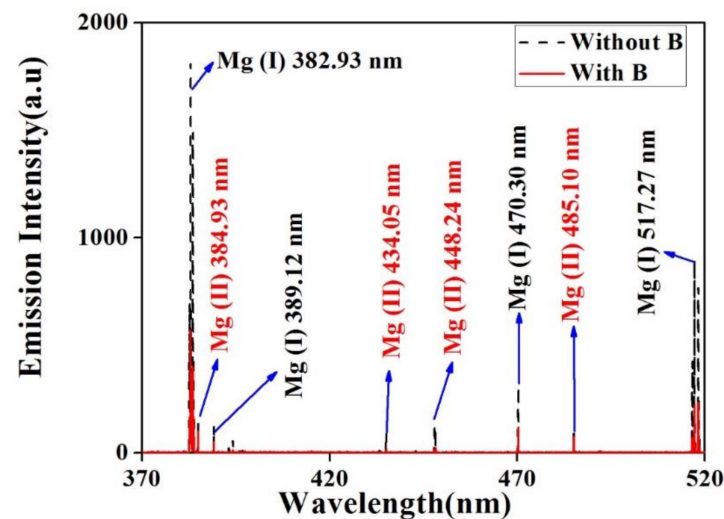

Figure 2. The emission spectra of selected Mg lines under 5 Torr pressure of Ar gas at 2 GW/cm^2 irradiance with and without TMF in the spectral range from 370 nm to 520 nm.

3.1.1. Investigation of Spectral Intensity of Mg Alloy Plasma

The graphs in Figure 3a,c,e illustrate the variation in the spectral intensities of chosen lines of Mg alloy in the absence of TMF, while Figure 3b,d,f illustrates the variations in spectral intensities of Mg alloy in the presence of TMF. All measurements were performed under variety of environments, i.e., Ar (a and b), Ne (c and d), and He (e and f) at 2 GW/cm^2 intensity and filled at different pressures. In the field-free scenario, the spectral intensity of the Mg alloy first rises and attains its maximum at 5 Torr, then subsequently drops with further increases in pressure. Additionally, it can be noticed that the emission intensity is significantly decreased in the presence of TMF as compared to the field-free scenario. This is true in all cases. The emission intensity value is higher in Ar, moderate in Ne, and lowest in He. It has been reported by several research groups that this decrease can be attributed to the combination of deceleration and enhanced radiation recombination [15,21–25]. The decrease in spectral intensity is due to a decrease in the lifetime of upper states attributed to strong magnetic confinement effects [23]. When TMF confines the plasma and restricts its free expansion, the lifetime for recombination is significantly decreased. As a consequence, the spectral intensity is decreased as well [10,24]. Another important reason for the reduction in spectral intensity of Mg lines is a decrease in the process of radiative recombination and an increase in the process of three-body radiative recombination [26]. When the laser pulse is over, three-body recombination prevails over radiative and/or dielectronic effects owing to the rapid decrease in T$_{exc}$. As the plasma expands, the lifetime

for recombination decreases significantly, resulting in a decrease in spectral intensity when the TMF is present relative to the field-free case [10,27].
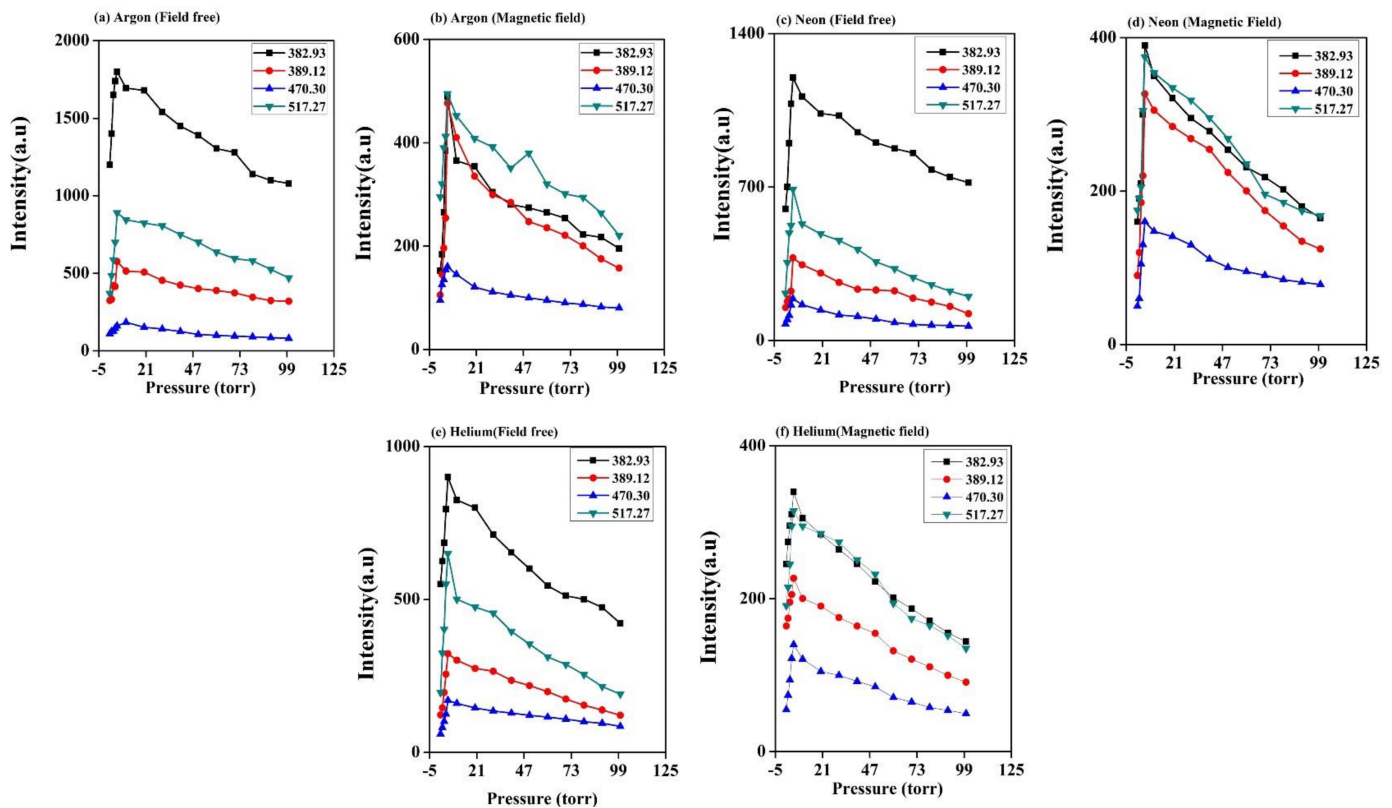

Figure 3. The spectral intensity variation of laser-induced Mg alloy plasma under several pressure levels of the inert gases Ar (**a**,**b**), Ne (**c**,**d**), and He (**e**,**f**) at 2 GW/cm^2 irradiance.

3.1.2. Evaluation of Excitation Temperature of Mg Alloy Plasma

To determine the T_{exc} of Mg plasma, the Boltzmann plot method was employed [23,28]. The Laser Induced Plasma (LIP) is assumed to be in Local Thermodynamic Equilibrium (LTE). The Boltzmann plot ($\ln\left(\frac{\lambda_{mn} I_{mn}}{g_m A_{mn}}\right) = -\left(\frac{E_m}{K T_{exc}}\right) + \ln\left(\frac{N(T)}{U(T)}\right)$) was used to calculate T_{exc} using spectroscopic data. Here, λ_{mn}, I_{mn}, g_m, and A_{mn} represent the wavelength, intensity of the higher energy state m, statistical weight, and transition probability, respectively. On the right side, E_m, k, T_{exc}, N (T), and U (T) represent the energy of the higher state, Boltzmann constant, excitation temperature, total number density, and partition function, respectively. The Boltzmann plot of the chosen lines is taken from the previously reported research work of Dawood et al. [28].The spectroscopic parameters necessary for T_{exc} analysis were acquired from the NIST database [29], atomic transition probabilities of sodium and magnesium. A critical compilation [30] and the atomic line list [31], and are listed in Table 1. The graphs of Figure 4a with Figure 4b without TMF illustrate the change in T_{exc} for various ambient gases at various pressures ranging from 1 to 100 Torr at a constant irradiance of 2 GW/cm^2. In the absence of TMF, the T_{exc} of Mg plasma varies between 9669 K and 13,730 K for Ar, 9327 K and 13,377 K for Ne, and 8793 K and 12,774 K for He. With the TMF applied, T_{exc} values for Ar vary from 10,814 K to 15,808 K, for Ne from 10,240 K to 15,370 K, and for He from 8876 K to 15,130 K. T_{exc} grows with increasing pressure in all situations with or without the TMF, and reaches at maximum at 5 Torr. The T_{exc} then decreases from 10 Torr to 100 Torr. In comparison to Ne and He, the highest T_{exc} value of Mg plasma is associated with Ar both in the presence and absence of TMF. Under all experimental conditions, we found that the use of TMF has a considerable influence on the enhancement of the T_{exc} of Mg plasma under various pressures of Ar, Ne, and He

environments at a laser irradiance of 2 GW/cm^2 in the absence (a) and presence (b) of the TMF.

Table 1. Spectroscopic parameters of Mg I lines obtained from the NIST Database and the existing literature [28].

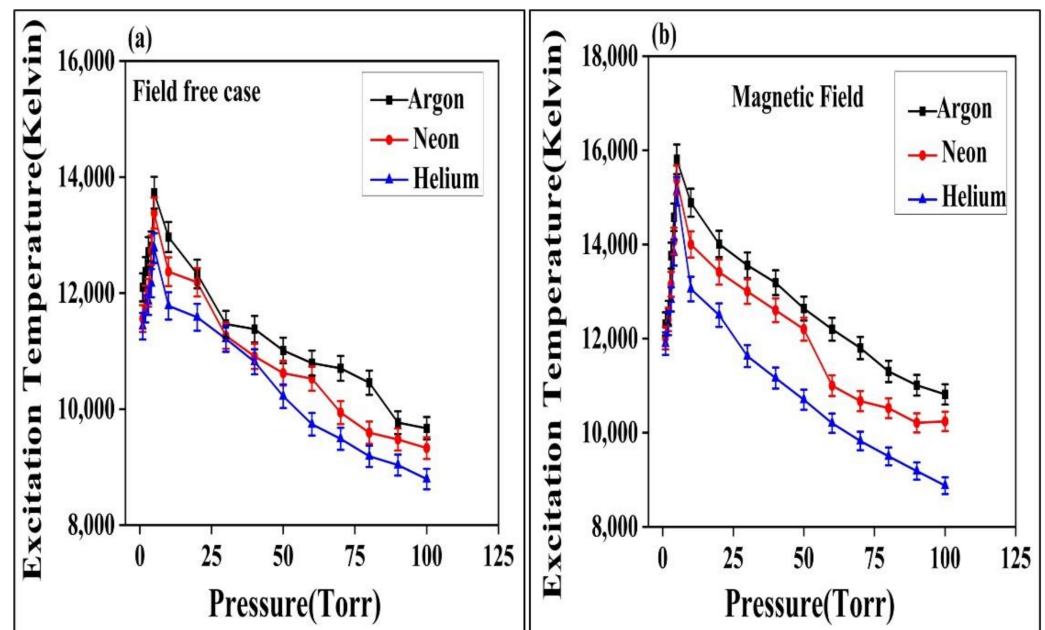| Wavelength (nm)	Transitions	Terms	Energy of Upper Level Em (cm^{-1})	Statistical Weight g$_m$	Transition Probabilities (108 s^{-1})
382.93	3s3p–3s3d	3p^o–3D	47,957.06	3	0.9
389.12	3p^2–3p.3d	3P–3D^o	83,511.25	3	1.31
470.30	3s3p–3s5d	1p^o–1D	56,308	5	0.255
517.27	3s3p–3s4s	3p^o–3S	41,197	3	0.346

Figure 4. The variation in excitation temperature of laser-induced Mg alloy plasma at various pressures of Ar, Ne, and He environments at ns laser irradiance of 2 GW/cm^2 in the absence (**a**) and presence (**b**) of TMF.

3.1.3. Evaluation of Electron Number Density of Mg Alloy Plasma

The Stark broadening method ($\Delta\lambda_{\frac{1}{2}} = 2\omega\left(\frac{N_e}{10^{16}}\right) + 3.5A\left(\frac{N_e}{10^{16}}\right)^{1/4}\left[1 - 1.2N_D^{-1/3}\right] \times \omega\left(\frac{N_e}{10^{16}}\right)$) was used to evaluate the time-integrated ne of Mg LPP [32,33]. In order to evaluate the n$_e$ of Mg alloy plasma, spectral line 517.27 nm of Mg (I) was chosen to apply Lorentzian fitting, with the Lorentzian fit graph taken from the previously reported research work of Dawood et al. [28].

Figure 5a,b shows the variation in ne of laser-produced Mg alloy plasma under different pressures of Ar, Ne, and He environments at 2.0 GW/cm^2 irradiance in the absence and presence of TMF, respectively. In the field-free situation, the n$_e$ of Mg plasma varies from 3.3×10^{17} cm^{-3} to 10.4×10^{17} cm^{-3} for Ar, from 3.2×10^{17} cm^{-3} to 9.8×10^{17} cm^{-3} for Ne, and from 1.0×10^{17} cm^{-3} to 9.4×10^{17} cm^{-3} for He. In the case with the TMF, ne varies from 7.9×10^{17} cm^{-3} to 10.6×10^{17} cm^{-3} for Ar, from 4.1×10^{17} cm^{-3} to 10.3×10^{17} cm^{-3} for Ne, and from 3.6×10^{17} cm^{-3} to 9.8×10^{17} cm^{-3} for He. From 1 to 4 Torr, the ne of Mg plasma rises linearly with pressure and reaches its maximum at 5 Torr; with further increase in pressure from 10 Torr to 100 Torr, n$_e$ decreases. This trend remains the same for the environmental gases Ar, Ne, and He. However, the n$_e$ of Mg plasma is again

higher in Ar than in Ne or He. Similarly, the significant enhancement effect of TMF on the ne of Mg plasma is observed under all conditions.
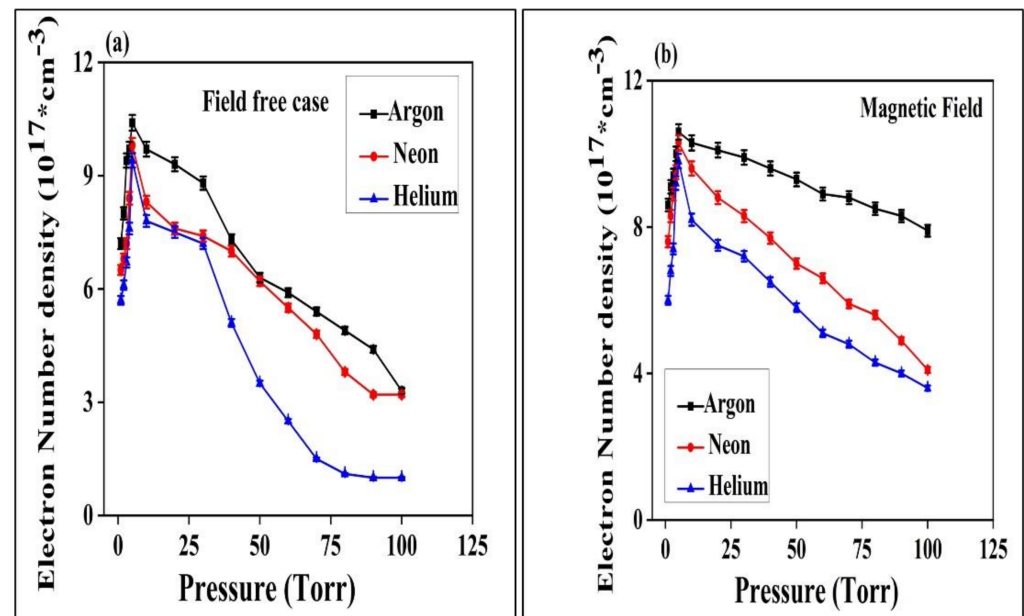

Figure 5. The variation in n_e of laser-induced Mg alloy plasma at various pressures under Ar, Ne, and He environments at an irradiance of 2.0 GW/cm^2 in the absence (**a**) and presence (**b**) of TMF.

4. Discussion

The trend of spectral intensity is distributed into three separate regions. In the first region, it increases as the background gas pressure rises. It then decreases with increasing pressure in the second region. Saturation is reached in the third region, without considerable fluctuation. All background gases display the same pattern in the presence and absence of a TMF. This initial rise in the spectral intensity of Mg alloy plasma with increasing ambient pressure from 1 to 4 Torr occurs owing to increased collisional excitation/de-excitation and spatial confinement, resulting in an enhanced ablation rate [1,34,35]. Due to the substantial confinement effect, the spectral intensity maximum is obtained at 5 torr. After that, a decrease in spectral intensity is observed. This decreasing tendency is due to a greater confinement impact of plasma species closer to the surface of the target, which produces a shielding effect. When the pressure is further raised up to 100 Torr, it results in saturation or a minimal change in spectral intensity, which is produced by the self-regulating regime. The recombination losses, plasma formation, and expansion processes are adjusted with each other in this regime, and no substantial change in intensity is noted.

Many research groups have reported that the features of LPP are highly dependent on the kind and pressure of the surrounding gases [36]. Plasma pressure is greater than the total pressure exerted by two confinements, such as the ambient and magnetic fields, at low environmental gas pressures of 1 to 2 Torr. As a result, the supersonic free expansion of the laser-produced expanding plasma occurs and a modest rising trend in both plasma properties is seen, which is attributed to the minor confinement effect [1]. Increases in the pressure of the surrounding environment from 3 to 4 Torr result in increased values for both plasma parameters. As the pressure is raised from 4 to 5 Torr, momentum transfer from the background gas to the plasma plume rises and the collisional frequency of plasma species increases, resulting in greater cascade development. Due to the radial and axial pushing pressures exerted by the background, a transition from the supersonic free zone to the shock-affected regime is effected, resulting in a slowdown of LPP propagation due to the compressional force exerted by the background gas. When the pressure exceeds 5 Torr, a decrease in T_{exc} and n_e can be noticed. This decrease in LPP parameters is caused by a decrease in the amount of laser energy absorbed by the target surface. Another potential

explanation for the drop in LPP parameters under increased pressure is the creation of laser-supported detonation waves which absorb the incoming laser light's, resulting into a large decrease in ablation rate. At greater pressures, less energy is absorbed by vapour plasma and more is absorbed by the shocked gas layer, resulting in a decrease in all plasma properties [37]. Due to the presence of surrounding gas at higher pressures, LPP rapidly cools [37]. At higher pressures, this decrease is owing to the increasing collisional frequency, which renders cascade growth undesirable [38]. The reason that Ar has greater T_{exc} and n_e values than Ne and He is because of cascade development and elastic collisions, as shown by the following relationship [38]:

$$Q_{\Delta t} = \frac{2m_e}{M_B} \sigma_{ea} n_B \left(\frac{5KT_e}{\pi m_e} \right)^{1/2} \tag{1}$$

where σ_{ea} denotes the elastic scattering cross-section of electron atoms, n_B represents the background gas atoms' density, and M_B denotes the background gas mass. According to Equation (1), M_B is inversely proportional to the cooling of LPP. It can be deduced from this relationship that lighter gases cool more quickly than heavier gases. With an increase in M_B, energy transfer through collision of particles becomes less effective, resulting in a longer life for LPP. The higher the thermal conductivity, the faster the LPP cools, resulting in a shorter plasma life [39]. The nature of environmental gases can have a major effect on plasma parameters. This tendency can be explained in terms of cascade development, with Iida et al. [5] having provided the essential conditions for cascade growth. They state in their article that only the E/M (charge/mass) ratio plays a significant role in determining the amount of energy lost during cascade development. The respective ratio in the case of Ar, Ne, and He is 0.53, 1.08, and 6.04. This demonstrates that cascade development is more favorable for Ar than for Ne or He. This explains why, in the case of Ar, Mg alloy plasma has a higher emission intensity, T_{exc}, and n_e than Ne and He plasma.

In all ambient gases, the T_{exc} and n_e values for Mg alloy with the TMF are greater than in the field-free situation. When plasma expands in the TMF, it is subjected to Lorentz force acting perpendicular to the direction of plume expansion, resulting in plasma species separation [1,33,40,41]. LPP is capable of propagating in both the axial and radial directions. Despite the fact that its velocity in the radial direction is less than its velocity in the axial direction, the LPP plasma front decelerates in both directions. Waheed et al. [18] proposed a slowdown of LPP in the presence of TMF. The thermal beta (β_t) can be calculated using Magneto hydrodynamic equations using the relationship proposed by Amin et al. [1]. When LPP pressure exceeds magnetic pressure by a factor of $\beta_t > 1$, there is no confinement because LPP penetrates the magnetic field region. Magnetic confinement is established under all experimental circumstances using both experimental and evaluation analytical values of β_t.

When both pressures equalize, i.e., $\beta_t = 1$, LPP is limited and begins to stagnate. When a TMF is applied to the LPP, it is confined inside a narrow region. This is due to the fact that the LPP is restrained by two forces: gas pressure provides one constraint, while the TMF provides the second. Figure 6 illustrates the β_t values for Mg alloy plasma. Tables 2–4 describe the changes in T_{exc}, n_e, and β_t for Mg alloy in the presence of the ambient gases Ar, Ne, and He, respectively. The examined results indicate that the T_{exc} and n_e values for Mg alloy are greater with the TMF than in the field-free situation, independent of the surrounding gases.
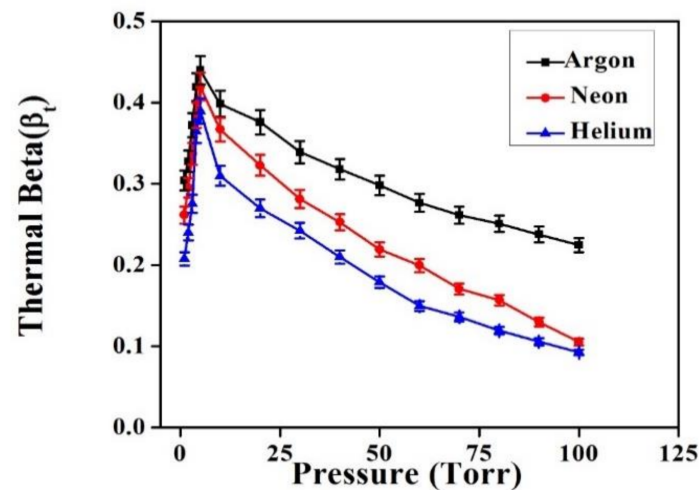
Figure 6. The variation in thermal beta of laser-induced Mg alloy plasma at various pressures under Ar, Ne, and He environments at ns laser irradiance of 2 GW/cm^2.

Table 2. Evaluated T_{exc}, n_e, and β_t values for laser-irradiated Mg plasma at various Ar pressures in the presence and absence of TMF.

| | Argon | | | | |
Pressure (Torr)	Excitation Temp (Field Free Case) (Kelvin)	Excitation Temp (Magnetic Field) (Kelvin)	n_e (10^{17}) (Field Free Case) (cm^{-3})	n_e (10^{17}) (Magnetic Field) (cm^{-3})	Thermal Beta
1	12,098	12,311	7.2	8.6	0.30
2	12,371	12,548	8.0	9.1	0.33
3	12,711	13,762	9.4	9.4	0.37
4	12,805	14,576	9.7	10.0	0.42
5	13,730	15,808	10.4	10.6	0.44
10	12,964	14,886	9.7	10.3	0.40
20	12,328	14,009	9.3	10.1	0.38
30	11,464	13,558	8.8	9.9	0.34
40	11,378	13,187	7.3	9.6	0.32
50	11,010	12,638	6.3	9.3	0.30
60	10,792	12,199	5.9	8.9	0.28
70	10,702	11,800	5.4	8.8	0.26
80	10,454	11,301	4.9	8.5	0.25
90	9765	11,010	4.4	8.3	0.24
100	9669	10,814	3.3	7.9	0.22

4.1. Validity of Magnetic Confinement

To verify that magnetic confinement is valid under all experimental circumstances, LPP of an Mg alloy target was captured at different delay times of 0.42, 0.83, 1.25, 1.67, 2.08, 2.50, 2.92, 3.33, 3.75, 4.58, 5.42, 6.25, 7.08, 7.92, 8.75, and 9.58 μs. Mg LPP was created for this purpose under varied environments of ambient Ar, Ne, and He at a fixed pressure of 5 Torr and a laser irradiance of 2.0 GW/cm^2. Figure 7 illustrates the fluctuation in T_{exc} of Mg plasma at various time delays with and without TMF. In the absence of TMF, the T_{exc} in Ar varies from 16,555 K to 9854 K, while in Ne it varies from 14,560 K to 9552 K and in He it changes from 13,875 K to 9258 K. In the presence of TMF, T_{exc} varies from 17,259 K to 11,548 K in Ar, 16,659 K to 10,787 K in Ne, and 16,541 K to 9616 K in He, with a temporal delay of 0.42 to 9.58 μs. Additionally, it is evident that Ar has the highest T_{exc} value compared to the other environmental gases. T_{exc} is greater in the presence than in the absence of the TMF.

Table 3. Evaluated T_{exc}, n_e, and β_t values for laser-irradiated Mg plasma at various Ne pressures in the presence and absence of TMF.

		Neon			
Pressure (Torr)	Excitation Temp (Field Free Case) (Kelvin)	Excitation Temp (Magnetic Field) (Kelvin)	n_e (10^{17}) (Field Free Case) (cm^{-3})	n_e (10^{17}) (Magnetic Field) (cm^{-3})	Thermal Beta
1	11,559	12,011	6.5	7.6	0.26
2	11,888	12,405	6.8	8.3	0.29
3	12,004	13,152	7.2	8.9	0.33
4	12,737	14,072	8.4	9.5	0.38
5	13,377	15,370	9.8	10.3	0.42
10	12,367	14,000	8.3	9.6	0.36
20	12,185	13,414	7.6	8.8	0.32
30	11,262	13,000	7.4	8.3	0.28
40	10,908	12,600	7.0	7.7	0.25
50	10,618	12,200	6.2	7.0	0.21
60	10,524	11,000	5.5	6.6	0.19
70	9939	10,671	4.8	5.9	0.17
80	9593	10,521	3.8	5.6	0.15
90	9476	10,210	3.2	4.9	0.12
100	9327	10,240	3.2	4.1	0.10

Table 4. Evaluated T_{exc}, n_e, and β_t values for laser-irradiated Mg plasma at various He pressures in the presence and absence of TMF.

		Helium			
Pressure (Torr)	Excitation Temp (Field Free Case) (Kelvin)	Excitation Temp (Magnetic Field) (Kelvin)	n_e (10^{17}) (Field Free Case) (cm^{-3})	n_e (10^{17}) (Magnetic Field) (cm^{-3})	Thermal Beta
1	11,428	11,893	5.7	6.0	0.20
2	11,728	12,319	6.1	6.8	0.24
3	11,859	12,831	6.7	7.4	0.27
4	12,169	13,826	7.6	9.2	0.36
5	12,774	15,130	9.4	9.8	0.39
10	11,779	13,051	7.8	8.2	0.30
20	11,581	12,498	7.5	7.5	0.27
30	11,211	11,628	7.2	7.2	0.24
40	10,814	11,160	5.1	6.5	0.21
50	10,222	10,700	3.5	5.8	0.17
60	9739	10,202	2.5	5.1	0.14
70	9487	9825	1.5	4.8	0.13
80	9186	9497	1.1	4.3	0.11
90	9034	9185	1.0	4.0	0.10
100	8793	8876	1.0	3.6	0.09

Figure 7 reveals that plasma temperature is significantly high in the early stages of plasma growth and rapidly decreases at later stages. This is because the plasma emission is first dominated by continuous emission generated by the plasma's bremsstrahlung and recombination emissions. Bremsstrahlung emission is sometimes referred to as free–free radiation due to the fact that it is generated by emission of charged particles. Additionally, recombination emission occurs as a consequence of free electrons being captured by ions. At early times, the plasma cools rapidly to very low temperatures, where it may remain stable for longer periods of time [42].
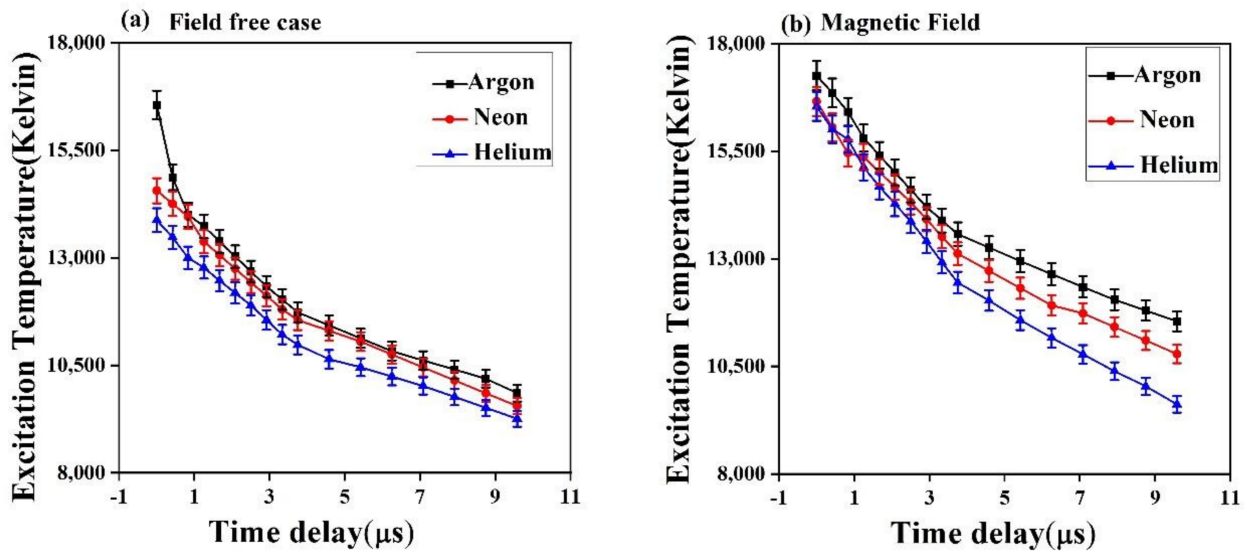
Figure 7. The variation of T_{exc} of LPP of Mg at different time delays in (**a**) the absence and (**b**) the presence of a magnetic field under Ar, Ne, and He.

Figure 8 illustrates the fluctuation in the n_e of Mg plasma at various time delays with and without TMF. Without TMF, the ne of Mg plasma varies from 11.2×10^{17} cm^{-3} to 7.05×10^{17} cm^{-3} in Ar, from 10.3×10^{17} cm^{-3} to 6.75×10^{17} cm^{-3} in Ne, and from 9.9×10^{17} cm^{-3} to 6.45×10^{17} cm^{-3} in He, whereas it ranges from 11.5×10^{17} cm^{-3} till 8.41×10^{17} cm^{-3} in Ar, 10.54×10^{17} cm^{-3} to 7.5×10^{17} cm^{-3} in Ne, and 10.2×10^{17} cm^{-3} till 7.0×10^{17} cm^{-3} in He when a TMF is used. These data indicate that ne reduces exponentially as the time delay increases.

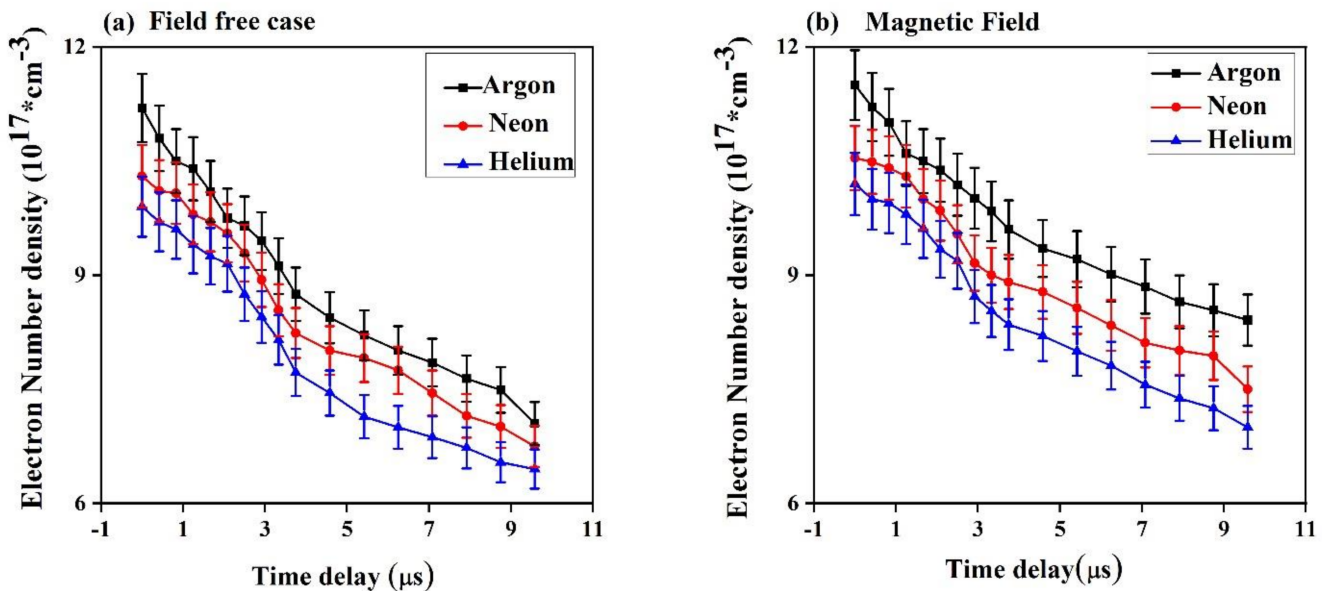**Figure 8.** The variation in electron number density of LPP of Mg alloy at different time delays in (**a**) the absence and (**b**) the presence of a magnetic field.

The reason for these plasma characteristics is attributed to the fact that the plasma initially expands isothermally during the laser pulse interaction. After the laser pulse is over and no more energy is being delivered into the plasma, T_{exc} decays rapidly throughout the delay period. At this stage, thermal energy is converted to directed kinetic energy, and the plasma cools as a result of adiabatic expansion [35]. LPP parameters exhibit a

t^{-2} dependency on time during the early phases of plasma production, which is consistent with Rumbsy and Paul's theoretical model [43]. According to Rumbsy and Paul [43], the relation $n_e \geq \frac{3 \times 10^{19} T_{exc}^{3.75}}{Z}$ m^{-3} demonstrates that if the estimated ne is greater than $\frac{3 \times 10^{19} T_{exc}^{3.75}}{Z}$ m^{-3}, three-body recombination prevails over radiative recombination. Our experimental values of n_e of Mg plasma are in the range of 10^{23} m^{-3}; these values are significantly higher than analytical evaluation, which is in range of 10^{19} m^{-3}. This indicates that when a TMF is used, three-body recombination takes priority over irradiative recombination, confirming the validity of three-body recombination and supporting the case for decreased spectral intensity after employment of TMF. The values of evaluated β_t at different time delays are shown in Figure 9 and tabulated in Tables 5–7 along with T_{exc} and n_e values for Mg plasma under Ar, Ne, and He.
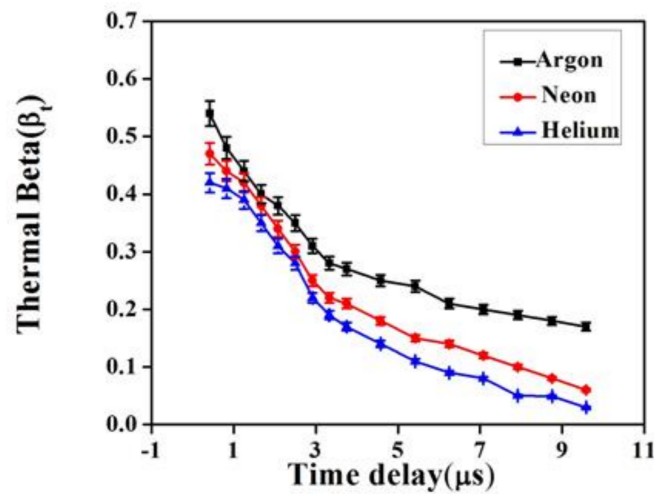

Figure 9. The variation in thermal beta at different time delays.

Table 5. Evaluated values of excitation temperature, electron number density, and thermal beta for LPP of Mg under Ar environment at different time delays with and without TMF.

Time Delay (µs)	Excitation Temp (Field Free Case) (Kelvin)	Excitation Temp (Magnetic Field) (Kelvin)	n_e (10^{17}) (Field Free Case) (cm^{-3})	n_e (10^{17}) (Magnetic Field) (cm^{-3})	Thermal Beta
		Argon			
0.42	14,870	16,858	10.8	11.21	0.54
0.83	14,005	16,420	10.5	11.01	0.48
1.25	13,730	15,808	10.4	10.6	0.44
1.67	13,380	15,408	10.1	10.5	0.4
2.08	13,030	15,008	9.75	10.38	0.38
2.50	12,680	14,608	9.65	10.19	0.35
2.92	12,330	14,208	9.45	10.01	0.31
3.33	12,030	13,893	9.12	9.84	0.28
3.75	11,730	13,578	8.75	9.6	0.27
4.58	11,430	13,263	8.44	9.35	0.25
5.42	11,130	12,948	8.21	9.21	0.24
6.25	10,830	12,648	8.01	9.01	0.21
7.08	10,616	12,348	7.85	8.85	0.2
7.92	10,402	12,048	7.64	8.65	0.19
8.75	10,188	11,798	7.49	8.54	0.18
9.58	9854	11,548	7.05	8.41	0.17

Table 6. Evaluated values of excitation temperature, electron number density, and thermal beta for LPP of Mg under Ne environment at different time delays with and without TMF.

Time Delay (μs)	Neon Excitation Temp (Field Free Case) (Kelvin)	Excitation Temp (Magnetic Field) (Kelvin)	n_e (10^{17}) (Field Free Case) (cm^{-3})	n_e (10^{17}) (Magnetic Field) (cm^{-3})	Thermal Beta
0.42	14,255	16,059	10.11	10.49	0.47
0.83	13,955	15,459	10.08	10.41	0.44
1.25	13,377	15,370	9.8	10.30	0.42
1.67	13,062	15,020	9.7	10.00	0.38
2.08	12,747	14,670	9.55	9.85	0.34
2.50	12,432	14,320	9.29	9.54	0.30
2.92	12,117	13,920	8.94	9.16	0.25
3.33	11,802	13,520	8.54	9.00	0.22
3.75	11,552	13,120	8.24	8.91	0.21
4.58	11,302	12,720	8.01	8.78	0.18
5.42	11,052	12,320	7.91	8.57	0.15
6.25	10,752	11,920	7.75	8.34	0.14
7.08	10,452	11,732	7.45	8.11	0.12
7.92	10,152	11,417	7.15	8.01	0.10
8.75	9852	11,102	7.01	7.94	0.08
9.58	9552	10,787	6.75	7.5	0.06

Table 7. Evaluated values of excitation temperature, electron number density, and thermal beta for LPP of Mg under He environment at different time delays with and without TMF.

Time Delay (μs)	Helium Excitation Temp (Field Free Case) (Kelvin)	Excitation Temp (Magnetic Field) (Kelvin)	n_e (10^{17}) (Field Free Case) (cm^{-3})	n_e (10^{17}) (Magnetic Field) (cm^{-3})	Thermal Beta
0.42	13,475	16,012	9.7	10.0	0.42
0.83	13,001	15,782	9.6	9.95	0.41
1.25	12,774	15,130	9.4	9.80	0.39
1.67	12,470	14,680	9.25	9.61	0.35
2.08	12,184	14,278	9.15	9.34	0.31
2.50	11,894	13,876	8.75	9.19	0.28
2.92	11,554	13,406	8.45	8.72	0.22
3.33	11,214	12,919	8.15	8.53	0.19
3.75	10,974	12,449	7.72	8.35	0.17
4.58	10,644	12,031	7.45	8.2	0.14
5.42	10,456	11,577	7.14	8.0	0.11
6.25	10,238	11,165	7.00	7.81	0.09
7.08	10,020	10,780	6.87	7.56	0.08
7.92	9766	10,390	6.73	7.38	0.05
8.75	9512	10,036	6.54	7.25	0.049
9.58	9258	9616	6.45	7.00	0.03

4.2. Surface Morphology

Mg alloy targets were irradiated at a fixed irradiance of 2 GW/cm^2 under 5 Torr pressure in Ar, Ne, and He, at which plasma parameters attain their maximum, in all ambient gases and both with and without TMF.

4.2.1. Surface Morphology under Ar Environment without TMF

Figure 10a–h show SEM micrographs of the laser-ablated areas of Mg under the Ar environment at a constant pressure of 5 Torr and a constant laser irradiance of 2.0 GW/cm^2 for the field-free case. Cones, cavities, and non-uniform melting are prominent features. Due to Gaussian distribution of the laser beam, the laser energy deposition at the central ablated areas is higher compared to the boundaries. The different micro-scale and

nano-scale surface structures are due to the Gaussian distribution of the laser pulse and non-uniform energy deposition to the target surface [44] at different regions.
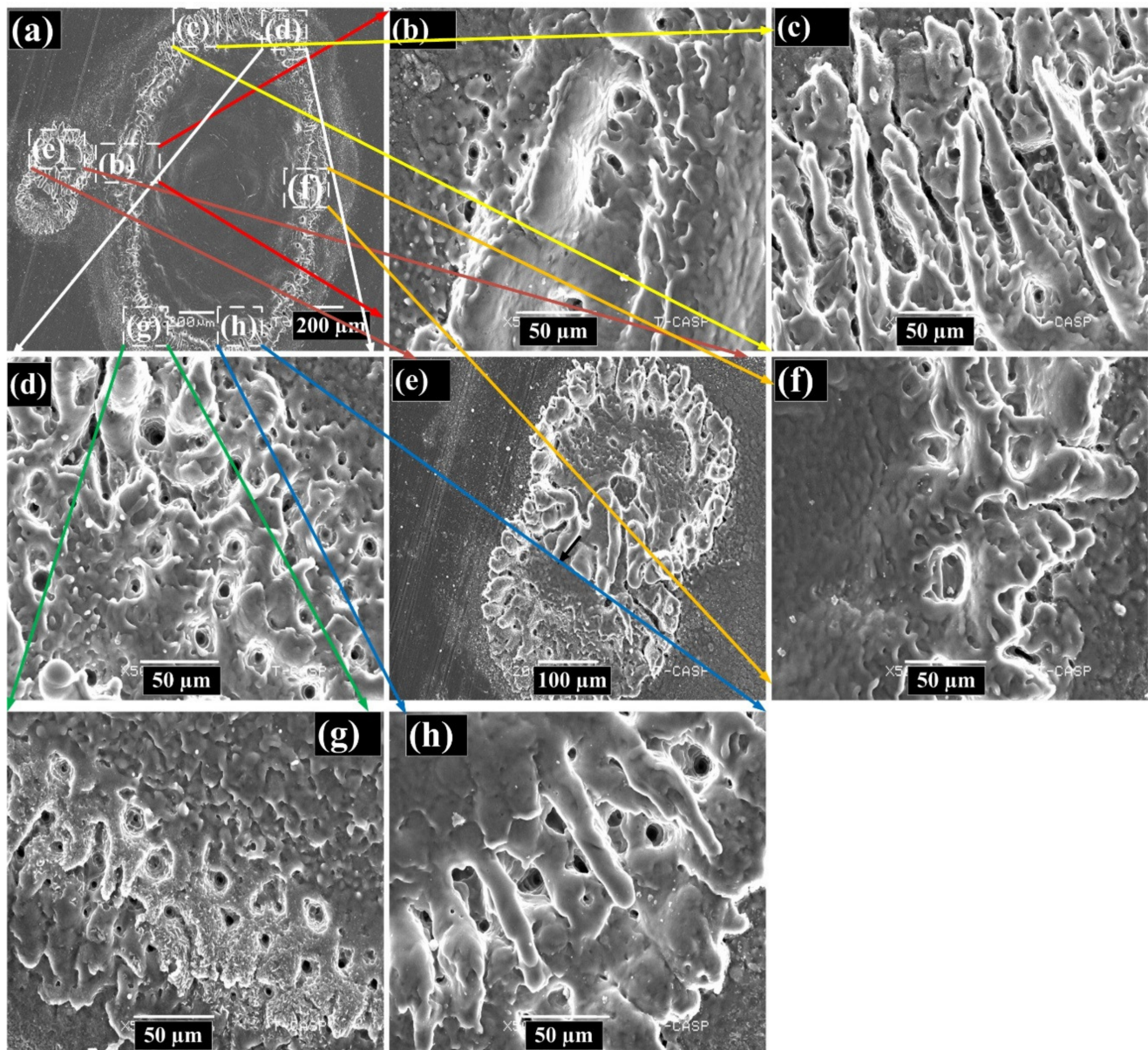

Figure 10. SEM micrographs exhibiting the variation in surface morphology under an ambient environment of Ar at a constant pressure of 5 Torr and a laser irradiance of 2.0 GW/cm^2 in the field-free case, where (**a**) laser-ablated crater on the Mg surface, (**b**) non-uniform melting of material and cavities at the boundary of the laser-ablated crater, (**c**) non-uniform micro-sized spikes and droplets at the laser-ablated crater, (**d**–**h**) various irregularly sized cones and cavities.

Figure 10a exhibits the laser-ablated crater on the Mg surface. The surface structuring can be seen at the boundaries, and molten metal can be seen at the centre of the ablated crater. Figure 10b shows the non-uniform melting of material and cavities at the boundary of the laser-ablated crater. Gases are absorbed after laser irradiation due to rapid volume expansion and heating of the subsurface layer, which is responsible for cavity formation [45]. Another possible reason for cavity formation may be the relaxation of mechanical stresses under the superficial layer [46]. Different sizes of cavities are due to contaminations, small pits, and inclusions on the target surface. Figure 10c shows non-uniform micro-sized

spikes and droplets. These spikes arise in two stages. In the first step, the incoming laser pulse causes the development of a depression as well as stresses on the target surface [47]. In the second step, when the laser pulse is over, the relaxation of these thermal stresses causes the evolution of spikes [47]. On the top of the spikes, tiny globules or round caps may be seen. In Figure 10d–h, irregularly sized cones and cavities can be observed. The growth of cones occurs in three steps. In the first step, before material processing, the generation of precursor sites due to micro/nano-scale laser-induced surface roughness and defects occurs [48]. In the second step, the incident laser light scatters from these sites. The increased preferential absorption of fluence along with the enhanced ablation rate at these sites between the valleys finally evolves into cones. The growth and merging of conical structures occur in the third step [49,50]. Figure 10e shows large craters and cones. Explosive relaxation of the mechanical stresses in the superficial layer may account for the formation of these craters [51].

4.2.2. Surface Morphology under Ar Environment with TMF

SEM images of Figure 11a–i show the laser ablated areas of Mg under Ar environment at a constant pressure of 5 Torr and a constant laser irradiance of 2.0 GW/cm^2 in the presence of TMF. Cones, caps of cones, and non-uniform melting are characteristic features. Figure 11a shows the laser-ablated surface at the boundaries and central areas. Figure 11b,c shows that micro-sized cones are formed at the periphery area of the laser-ablated crater. Figure 11d shows the centre of the laser-ablated crater, where the non-uniform melting is maximum due to maximum deposition of laser energy at the center. Droplets can be observed; droplet formation is considered to be due to hydrodynamical sputtering [52]. Volumetric heating occurs during laser matter interaction depending on the absorption coefficient and thermal diffusivity of the target surface. This heating and vaporization results in the production of a temperature gradient, which is responsible for the expansion of molten material in the form of droplets [53]. Figure 11e,f shows the left-hand side and right-hand side outer boundaries, respectively, of the ablated crater. Micro-sized cones and caps on the top of ridges can be observed. Figure 11g shows cavities and particulate formation. Figure 11h,i show the formation of micro-sized cones and spikes. The cones have a wider base and uplifted sharp edges, with certain uplifted sharp edges having caps on top of the cones.

4.2.3. Surface Morphology under Ne Environment without TMF

The SEM micrographs in Figure 12a–f reveal the different micro-structured laser-ablated areas of Mg under the Ne environment at a constant pressure of 5 Torr and a laser irradiance of 2.0 GW/cm^2 in the field-free case. Cones and cavities are characteristic features at all boundaries. Figure 12a shows the surface structure at the boundaries of the laser-ablated crater of the Mg alloy. Figure 12b–d shows the cones and irregularly sized cavities at the left, upper, and right side outer boundary, respectively, of the ablated crater. Irregular ridges can be observed at the bottom of the cones. When the laser energy exceeds the ablation threshold, plasma is formed due to the heating, melting, and vaporization of the target material. When the plasma pressure exceeds the surrounding pressure, the molten material is expelled explosively from the target surface due to the recoil pressure, accounting for the periodic ridges [54]. Another possible reason for ridge formation is the enhanced recoil pressure of the plasma, which splashes molten material towards the boundary [55]. Figure 12e shows a small circular crater near the large laser-ablated crater. Cones, caps on the top of cones, and droplets are the main features. Micro-sized ridges and cavities can be observed at the lower outer boundary of the crater in Figure 12f.
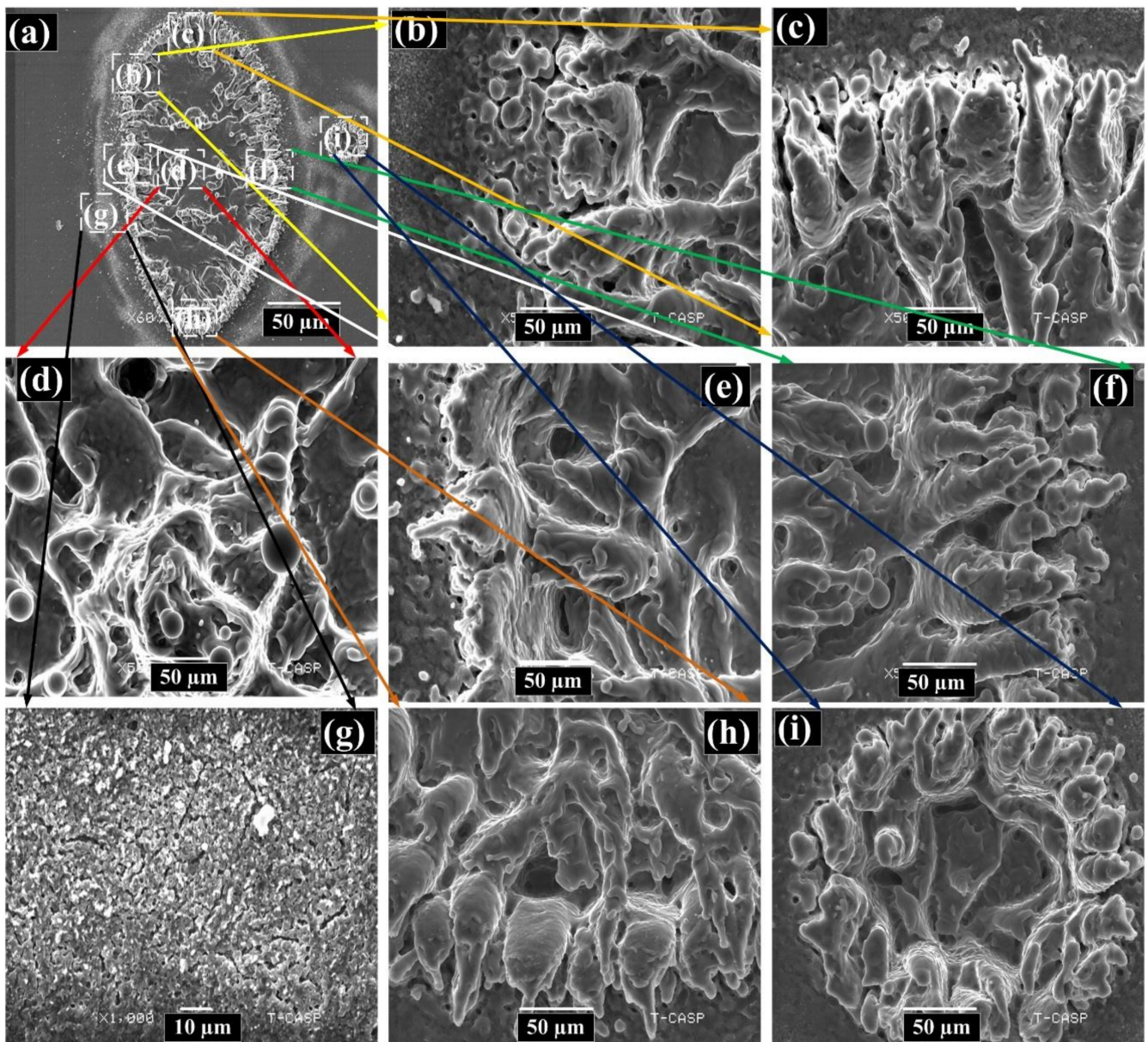
Figure 11. SEM images illustrating the surface morphology of the laser-ablated areas of Mg under an ambient environment of Ar at a constant pressure of 5 Torr and a laser irradiance of 2.0 GW/cm^2 in magnetic field where (**a**) laser ablated areas of Mg at the boundaries and central areas, (**b**) 1st sample of micro-sized cones are formed at the periphery area of the laser-ablated crater, (**c**) 2nd sample of micro-sized cones are formed at the periphery area of the laser-ablated crater, (**d**) Droplets at laser-ablated crater due to maximum deposition of laser energy at the center, (**e**) left-hand side outer boundaries at laser ablated crater (**f**) right-hand side outer boundaries at laser ablated crater (**g**) cavities and particulate formation at laser-ablated crater, (**h**) micro-sized cones, and (**i**) micro-sized spikes.
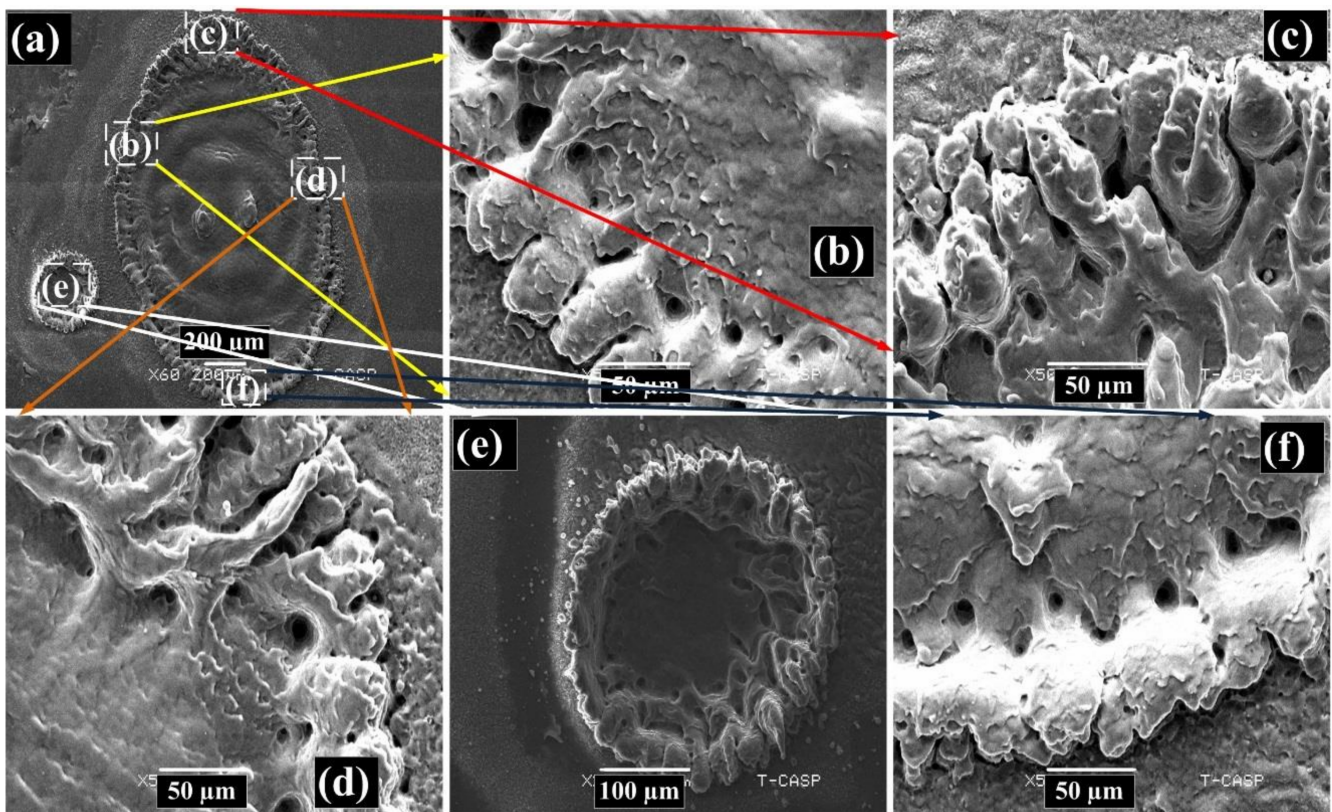
Figure 12. SEM micrographs of the laser-ablated areas of Mg showing the variation in surface morphology under an ambient environment of Ne and a constant pressure of 5 Torr for a laser irradiance of 2.0 GW/cm^2 in the field-free case, where (**a**) the surface structure at the boundaries of the laser-ablated crater of the Mg alloy, (**b**) the cones and irregularly sized cavities at the left side, (**c**) the cones and irregularly sized cavities at the upper side, (**d**) the cones and irregularly sized cavities at the right side of laser-ablated crater, (**e**) small circular crater near the large laser-ablated crater, (**f**) Micro-sized ridges and cavities can be observed at the lower outer boundary of the crater.

4.2.4. Surface Morphology under Ne Environment with TMF

Figure 13a–g presents SEM micrographs for various surface features on laser-ablated areas of Mg under Ne environment at a constant pressure of 5 Torr and a laser irradiance of 2.0 GW/cm^2 in the magnetic field case. Spike-shaped cones, cavities, and grains are characteristic features at all boundaries. Figure 13a shows the surface structure at the boundaries of the laser ablated-crater of the Mg alloy. Figure 13b–d shows micro-sized conical spikes in the periphery areas, and cavities can be seen as well. A top view of conical spikes is shown in Figure 13e. The uplifted conical spikes are forward-peaked. Flakes have formed at the lower boundary of the ablated crater in Figure 13f, and irregular micro-sized flakes with distinct boundaries can be observed. Exfoliational sputtering following laser irradiation is the basic mechanism responsible for flake formation. Temperature and pressure gradients are produced due to fast heating and cooling, which generate residual stresses in the surface layer. Preferential crystallization and grain-like structures are generated due to localized heating and cooling [56,57]. Figure 13g shows the non-uniform melting and resulting dendritic structures.
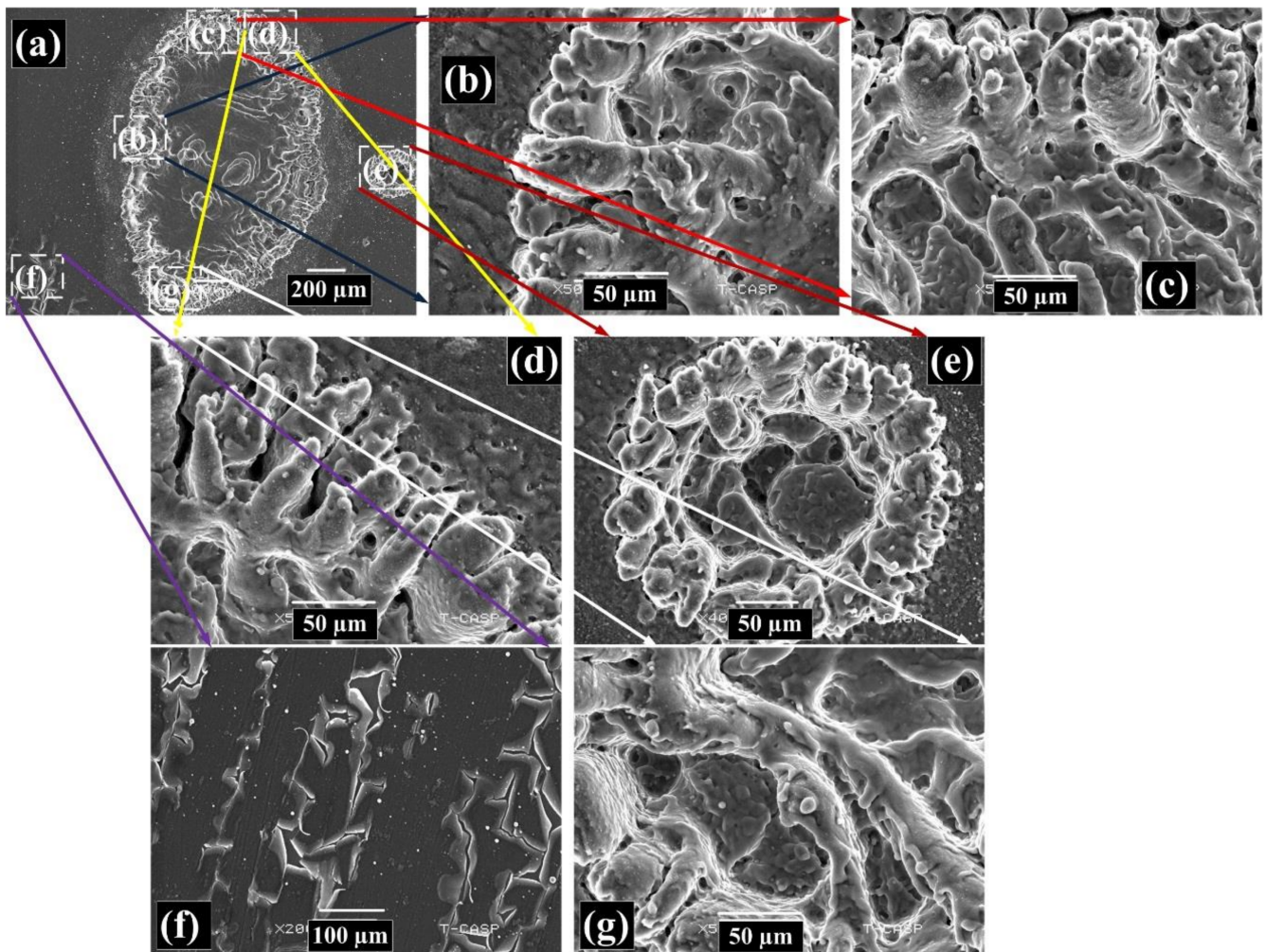
Figure 13. SEM images revealing the surface morphology of laser-irradiated Mg at constant pressure of 5 Torr of Ne gas and laser irradiance of 2.0 GW/cm^2 in the presence of a magnetic field, where (**a**) the surface structure at the boundaries of the laser ablated-crater of the Mg alloy, (**b–d**) sample micro-sized conical spikes and cavities in the periphery areas, (**e**) A top view of conical spikes, (**f**) flakes at the lower boundary of the ablated crater, and (**g**) non-uniform melting and resulting dendritic structures.

4.2.5. Surface Morphology under He Environment without TMF

Figure 14a–e exhibits SEM micrographs of the laser-ablated areas of Mg at 5 Torr constant pressure under He environment at a constant laser irradiance of 2.0 GW/cm^2 in the field-free case. Conical spikes and cavities are characteristic features in all boundary areas. The laser-ablated crater of the Mg can be seen in Figure 14a. Figure 14b shows a small crater near the main laser-ablated area. Upward-lifted cones can be seen at the edges along with molten material and cavities at the centre. Non-uniform cones with cavities can be seen in Figure 14c, with small cavities on the cones. Forward-peaked cones with wide bases and spherical caps on top can be observed in Figure 14d. Figure 14e shows the turbulent melt flow of molten material towards the outer boundary along with the formation of cavities and conical spikes.
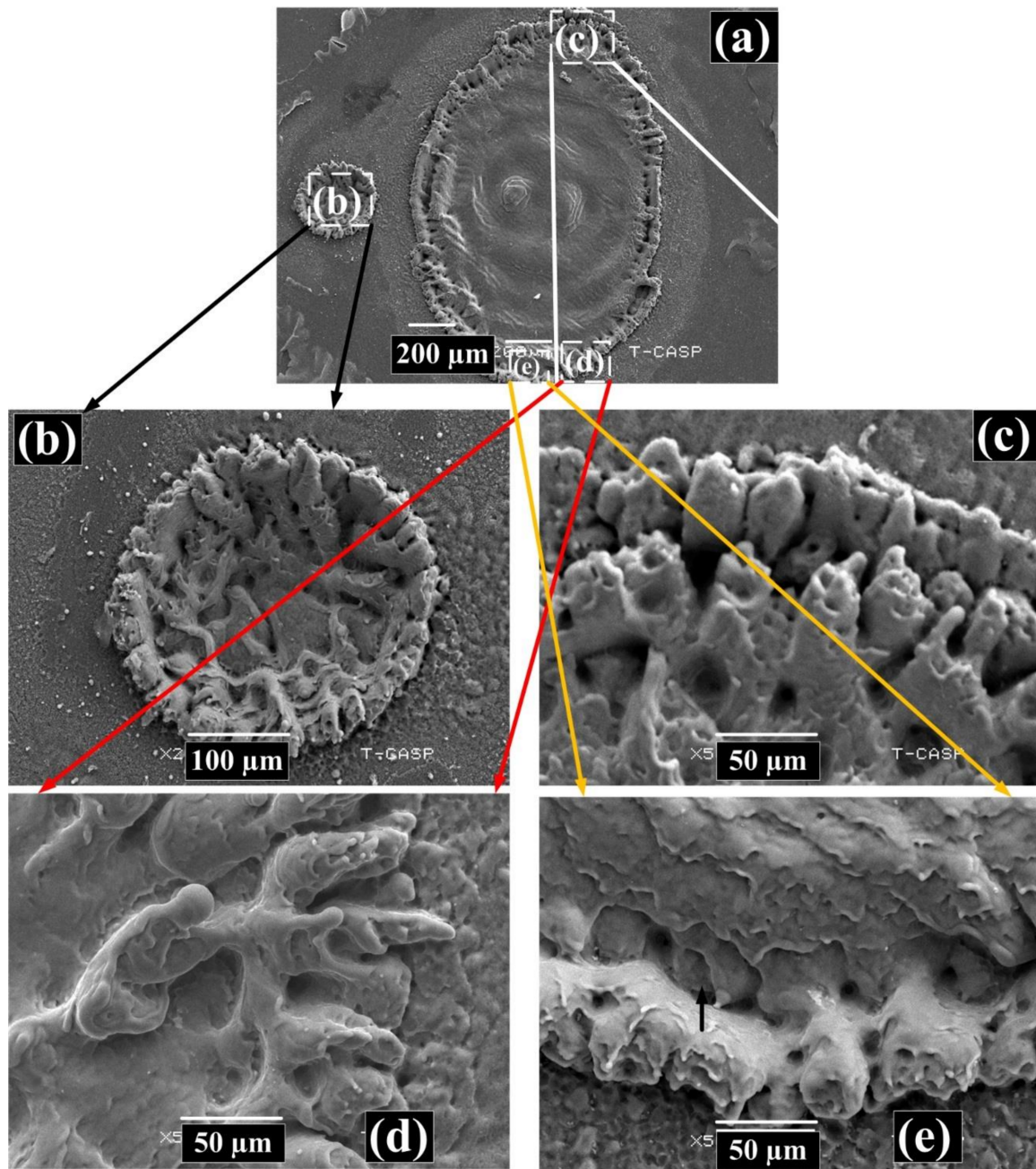
Figure 14. SEM images of the laser-irradiated areas of Mg showing the different surface features under He ambient environment at a constant pressure of 5 Torr and laser irradiance of 2.0 GW/cm^2 in the magnetic field-free case, where (**a**) laser-ablated crater of the Mg, (**b**) small crater near the main laser-ablated area, (**c**) non-uniform cones with cavities on the cones, (**d**) forward-peaked cones with wide bases and spherical caps on top, and (**e**) cavities and cones due to turbulent melt flow of molten material towards the outer boundary.

4.2.6. Surface Morphology under He Environment with TMF

Figure 15a–f shows SEM micrographs of the laser-ablated area of Mg at a constant pressure of 5 Torr under ambient environment of He at a constant laser irradiance of 2.0 GW/cm^2 in the magnetic field case. Non-uniform melting, cavities, conical protrusions, and dendrite are characteristic features at all boundary areas. Figure 15a shows the laser-ablated crater of the Mg alloy. The left-hand outer boundary and right-hand outer boundary of the laser ablated crater show dendritic structures, cavities, and conical protrusions in the Figure 15b,c. Figure 15d,e exhibits dendritic structures, turbulent melt flow towards the

outer boundary, and cavities at the upper and lower outer boundary of the laser ablated crater. Figure 15f shows a micro-sized crater which exhibits forward peaked cones.
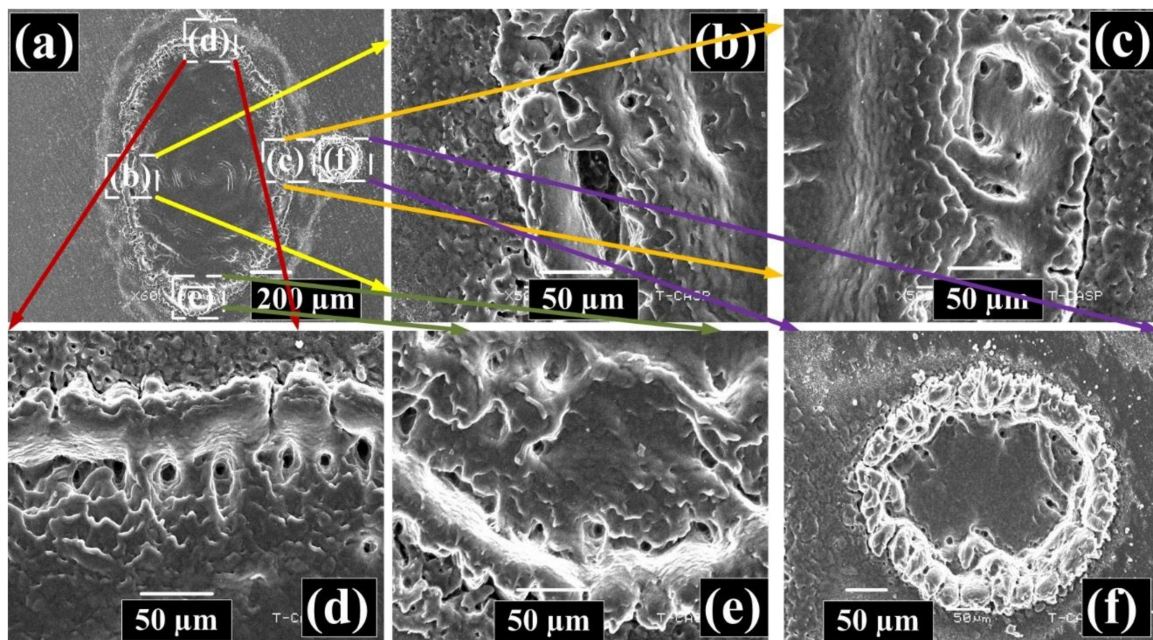

Figure 15. SEM micrographs of the laser irradiated areas of Mg exhibiting the surface morphology under ambient environment of He at a constant pressure of 5 Torr and laser irradiance of 2.0 GW/cm^2 in the presence of a magnetic field, where (**a**) laser-ablated crater of the Mg alloy, (**b**) dendritic structures, cavities, and conical protrusions at left-hand outer boundary (**c**) dendritic structures, cavities, and conical protrusions at right-hand outer boundary of the laser ablated, (**d**) dendritic structures, turbulent melt flow towards the outer boundary, and cavities at the upper outer boundary of the laser ablated crater, (**e**) dendritic structures, turbulent melt flow towards the outer boundary, and cavities at lower outer boundary of the laser ablated crater, and (**f**) micro-sized crater and forward peaked cones.

Figures 10 and 11 (in the Ar environment), Figures 12 and 13 (in the Ne environment), and Figures 14 and 15 (in the He environment) clearly reveal that diffusive craters are formed on the surface of the Mg alloy in the absence of a magnetic field, whereas structured craters with multiple distinct features are formed in the presence of the TMF. Similarly, at the boundaries there are sharp and uplifted cones along with distinct cavities formed in the absence of the TMF, whereas these cones are suppressed due to larger plasma recoil pressure with the TMF. Shock-liquefied material refills the cavities due to additional plasma recoil pressure, resulting in cavities that are less prominent in Ar and Ne. As LPP parameters are smaller in He as compared to Ar and Ne, the lower recoil pressure in He is responsible for cavity formation even in the presence of the TMF. In the case under Ne and with TMF, a clear feature that can be seen in Figure 13f is the presence of flakes. This generally happens only in high-melting-point materials; however, in this case the metallic surface of the Mg alloy tries to detach under the influence of exfoliational sputtering and is not fully detached, representing its moderate ablation at moderate plasma recoil pressure due to moderate plasma parameters.

Laser-induced plasma is one of best sources for thin film deposition and surface structuring of materials under different environments, and is a beneficial tool by which different kinds of micro-scale structures can be grown that are well correlated with plasma-induced plasma effects and recoil pressure. In this way, by controlling plasma parameters, it is possible to control surface structuring, coating by plasma, and coating by ion implantation on different materials.

5. Conclusions

In this paper, we investigated the significant effect of a TMF on Mg LPP parameters as a function of pressure in a variety of ambient environments, namely, Ar, Ne, and He. At a constant laser irradiance and time delay, it was found that Mg plasma parameters are greatly increased in the presence of a magnetic field as compared to the field-free case at all pressures and in all ambient environments. Magnetic confinement, Joule's heating, and adiabatic compression all contribute to the increase in LPP.

i. The emission intensity, excitation temperature, and electron number density of Mg plasmas are shown to be highly dependent on the ambient gas pressure. Initially, the T_{exc} and n_e values increase with increasing pressure, attain their maxima, and then decrease or become saturated. This is true under all environmental circumstances. The same trends for T_{exc} and n_e are found in the presence of TMF as well as in the absence of a field in all ambient conditions.

ii. The highest plasma parameters are obtained with the shortest delay duration. However, in all circumstances the spectral intensities T_{exc} and n_e are greater in the ambient Ar environment than in Ne and He. These findings related to Ar are due to its lower thermal conductivity and a greater rate of cascade development compared to Ne and He. Analytical evaluation of the value of thermal beta (β_t) for various ambient gas pressures shows that β_t is smaller than 1 for all cases, confirming the confinement of Mg plasma under a 1.1 T magnetic field.

iii. A structured crater is formed in the presence of the TMF, whereas in the absence of the TMF diffusive crater formation is observed. In the absence of the TMF, uplifted cones and cavities grow in all environmental conditions, whereas these cavities and cones are suppressed in the presence of the TMF due to enhanced plasma-induced effects and recoil pressure of the plasma.

iv. Magnetically-confined plasma can be more beneficial as an ion source with enhanced T_{exc} and n_e for ion implantation, thin film deposition, and coating of a variety of materials.

Author Contributions: Conceptualization, A.D., S.B. and A.H.; methodology A.D., S.B., A.H. and N.A.; experimentation, A.D., S.B. and A.H.; validation of data, A.D., S.B., A.H., S.M.A.S. and S.A.A.; formal analysis, A.D., S.B., A.H., S.M.A.S. and A.Y.A.; investigation, A.D., S.B., A.H., S.M.A.S., S.A.A. and N.A.; resources, A.D., S.B., A.H. and N.A.; writing—original draft preparation, A.D. and S.M.A.S.; writing—review and editing, A.D., S.B., A.H., N.A., A.Y.A., S.M.A.S., S.A.A. and A.U.R.; supervision, S.B., A.H., N.A., A.Y.A. and A.U.R.; project administration, A.D., S.B., A.H. and N.A.; All authors have read and agreed to the published version of the manuscript.

Institutional Review Board Statement: Not applicable.

Informed Consent Statement: Not applicable.

Data Availability Statement: Not applicable.

Conflicts of Interest: The authors declare no conflict of interest.

References

1. Amin, S.; Bashir, S.; Anjum, S.; Akram, M.; Hayat, A.; Waheed, S.; Iftikhar, H.; Dawood, A.; Mahmood, K. Optical emission spectroscopy of magnetically confined laser induced vanadium pentoxide (V2O5) plasma. *Phys. Plasmas* **2017**, *24*, 083112. [CrossRef]
2. Russo, R.; Mao, X.; Yoo, J.; Gonzalez, J. Laser ablation. In *Laser-Induced Breakdown Spectroscopy*; Elsevier: Oxford, UK, 2007; pp. 49–82.

3.   Chichkov, B.N.; Momma, C.; Nolte, S.; Von Alvensleben, F.; Tünnermann, A. Femtosecond, picosecond and nanosecond laser ablation of solids. *Appl. Phys. A* **1996**, *63*, 109–115. [CrossRef]

4.   Brown, M.S.; Arnold, C.B. Fundamentals of laser-material interaction and application to multiscale surface modification. In *Laser Precision Microfabrication*; Springer: Berlin/Heidelberg, Germany, 2010; pp. 91–120.

5.   Iida, Y. Effects of atmosphere on laser vaporization and excitation processes of solid samples. *Spectrochim. Acta B* **1990**, *45*, 1353–1367. [CrossRef]

6.   Miyaji, G.; Miyazaki, K. Origin of periodicity in nanostructuring on thin film surfaces ablated with femtosecond laser pulses. *Opt. Exp.* **2008**, *16*, 16265–16271. [CrossRef]

7.   Sakata, F.; Santo, A.; Miyakawa, W.; Riva, R.; Lima, M. Influence of laser surface texturing on surface microstructure and mechanical properties of adhesive joined steel sheets. *Surf. Eng.* **2009**, *25*, 180–186. [CrossRef]

8.   Vorobyev, A.; Guo, C. Femtosecond laser-induced periodic surface structure formation on tungsten. *J.Appl.Phys.* **2008**, *104*, 063523. [CrossRef]

9.   Neogi, A.; Thareja, R. Laser-produced carbon plasma expanding in vacuum, low pressure ambient gas and nonuniform magnetic field. *Phys. Plasmas* **1999**, *6*, 365–371. [CrossRef]

10.   Shen, X.; Lu, Y.; Gebre, a.T.; Ling, H.; Han, Y. Optical emission in magnetically confined laser-induced breakdown spectroscopy. *J. Appl Phys.* **2006**, *100*, 1–7. [CrossRef]

11.   Pandey, P.K.; Thareja, R.K. Plume dynamics and cluster formation in laser-ablated copper plasma in a magnetic field. *J. Appl. Phys.* **2011**, *109*, 074901. [CrossRef]

12.   Bashir, S.; Farid, N.; Mehmood, K.; Rafique, M.S. Influence of ambient gas and its pressure on the laser-induced breakdown spectroscopy and the surface morphology of laser-ablated Cd. *Appl. Phys. A* **2012**, *107*, 203–212. [CrossRef]

13.   Singh, K.S.; Sharma, A.K. Time-integrated optical emission studies on laser-produced copper plasma in the presence of magnetic field in air ambient at atmospheric pressure. *Appl. Phys. A* **2017**, *123*, 325. [CrossRef]

14.   Arshad, A.; Bashir, S.; Hayat, A.; Akram, M.; Khalid, A.; Yaseen, N.; Ahmad, Q.S. Effect of magnetic field on laser-induced breakdown spectroscopy of graphite plasma. *Appl. Phys. B* **2016**, *122*, 63. [CrossRef]

15.   Li, Y.; Hu, C.; Zhang, H.; Jiang, Z.; Li, Z. Optical emission enhancement of laser-produced copper plasma under a steady magnetic field. *Appl. Opt.* **2009**, *48*, B105–B110. [CrossRef]

16.   Ye, C.; Cheng, G.J.; Tao, S.; Wu, B. Magnetic field effects on laser drilling. *J. Manuf. Sci. Eng.* **2013**, *135*, 061020. [CrossRef]

17.   Abbasi, S.A.; Aziz, Z.; Khan, T.M.; Ali, D.; ul Hassan, T.; Iqbal, J.; Khan, S.U.-D.; Ahmad, A.; Khan, R.; Khan, E.M. Enhancement of optical signal and characterization of palladium plasma by magnetic field-assisted laser-induced breakdown spectroscopy. *Optik* **2020**, *224*, 165746. [CrossRef]

18.   Waheed, S.; Bashir, S.; Dawood, A.; Anjum, S.; Akram, M.; Hayat, A.; Amin, S.; Zaheer, A. Effect of magnetic field on laser induced breakdown spectroscopy of zirconium dioxide (ZrO 2) plasma. *Optik* **2017**, *140*, 536–544. [CrossRef]

19.   Aguilera, J.; Aragon, C. A comparison of the temperatures and electron densities of laser-produced plasmas obtained in air, argon, and helium at atmospheric pressure. *Appl. Phy. A* **1999**, *69*, S475–S478. [CrossRef]

20.   Hussain, A.; Asghar, H.; Iqbal, T.; Ishfaq, M.; Shahbaz, R.M.; Riaz, Q. Improving the spectral intensity of aluminum plasma by applied-magnetic field in laser-induced breakdown spectroscopy. *Optik* **2021**, *251*, 168220. [CrossRef]

21.   Singh, K.S.; Sharma, A.K. Multi-structured temporal behavior of neutral copper transitions in laser-produced plasma in the presence of variable transverse static magnetic field. *Phys. Plasmas* **2016**, *23*, 1–11. [CrossRef]

22.   Cheng, L.; Xun, G.; Qi, L.; Chao, S.; Jingquan, L. Spectral enhancement of laser-induced breakdown spectroscopy in external magnetic field. *Plasma Sci. Technol.* **2015**, *17*, 919–922.

23.   Iftikhar, H.; Bashir, S.; Dawood, A.; Akram, M.; Hayat, A.; Mahmood, K.; Zaheer, A.; Amin, S.; Murtaza, F. Magnetic field effect on laser-induced breakdown spectroscopy and surface modifications of germanium at various fluences. *Laser Part. Beams* **2017**, *35*, 159–169. [CrossRef]

24.   Joshi, H.; Kumar, A.; Singh, R.; Prahlad, V. Effect of a transverse magnetic field on the plume emission in laser-produced plasma: An atomic analysis. *Spectrochim. Acta B* **2010**, *65*, 415–419. [CrossRef]

25.   Kim, T.H.; Nam, S.H.; Park, H.S.; Song, J.K.; Park, S.M. Effects of transverse magnetic field on a laser-produced Zn plasma plume and ZnO films grown by pulsed laser deposition. *App. Surf. Sci* **2007**, *253*, 8054–8058. [CrossRef]

26.   Harilal, S.; Sizyuk, T.; Hassanein, A.; Campos, D.; Hough, P.; Sizyuk, V. The effect of excitation wavelength on dynamics of laser-produced tin plasma. *J. Appl. Phys.* **2011**, *109*, 063306. [CrossRef]

27.   Harilal, S.; Tillack, M.; O'shay, B.; Bindhu, C.; Najmabadi, F. Confinement and dynamics of laser-produced plasma expanding across a transverse magnetic field. *Phys. Rev. E* **2004**, *69*, 026413. [CrossRef] [PubMed]

28.   Dawood, A.; Bashir, S. Characterizing laser induced plasma and ablation of Mg-alloy in the presence and absence of magnetic field. *Optik* **2018**, *170*, 353–367.

29.   Kramida, A.; Olsen, K.; Ralchenko, Y. *Nist Libs Database*; National Institute of Standards and Technology, US Department of Commerce: Gaithersburg, MD, USA, 2019.

30.   Kelleher, D.E.; Podobedova, L. Atomic transition probabilities of sodium and magnesium. A critical compilation. *J. Phys. Chem. Ref. Data* **2008**, *37*, 267–706. [CrossRef]

31.   List, I.A. Atomic Line List v3.00b4. Available online: http://www.pa.uky.edu/~{}peter/newpage/ (accessed on 18 August 2021).

32. Nakimana, A.; Tao, H.; Camino, A.; Gao, X.; Hao, Z.; Lin, J. Effect of ambient pressure on femtosecond laser-induced breakdown spectroscopy of Al in argon. In Proceedings of the 2012 International Conference on Optoelectronics and Microelectronics, Changchun, China, 23–25 August 2012; pp. 146–150.

33. Dawood, M.; Margot, J. Effect of ambient gas pressure and nature on the temporal evolution of aluminum laser-induced plasmas. *Aip Adv.* **2014**, *4*, 037111. [CrossRef]

34. Hafeez, S.; Shaikh, N.M.; Rashid, B.; Baig, M.A. Plasma properties of laser-ablated strontium target. *J. Appl. Phys.* **2008**, *103*, 083117–083124. [CrossRef]

35. Harilal, S.S.; Bindhu, C.V.; Nampoori, V.P.N.; Vallabhan, C.P.G. Temporal and spatial behavior of electron density and temperature in a laser-produced plasma from YBa2Cu3O7. *Appl. Spectrosc.* **1998**, *52*, 449–455. [CrossRef]

36. Luo, W.; Zhao, X.; Sun, Q.; Gao, C.; Tang, J.; Wang, H.; Zhao, W. Characteristics of the aluminum alloy plasma produced by a 1064 nm Nd: YAG laser with different irradiances. *Pramana* **2010**, *74*, 945–959. [CrossRef]

37. Dawood, A.; Bashir, S.; Akram, M.; Hayat, A.; Ahmed, S.; Iqbal, M.H.; Kazmi, A.H. Effect of nature and pressure of ambient environments on the surface morphology, plasma parameters, hardness, and corrosion resistance of laser-irradiated Mg-alloy. *Laser Part. Beams* **2015**, *33*, 315–330. [CrossRef]

38. Farid, N.; Bashir, S.; Mehmood, K. Effect of ambient gas conditions on laser-induced copper plasma and surface morphology. *Phys. Scr.* **2012**, *85*, 015702–015709. [CrossRef]

39. Effenberger, A.J.; Scott, J.R. Effect of atmospheric conditions on LIBS spectra. *Sensors* **2010**, *10*, 4907–4925. [CrossRef]

40. Chishti, N.A.; Bashir, S.; Dawood, A.; Khan, M.A. Laser-induced breakdown spectroscopy of aluminum plasma in the absence and presence of magnetic field. *App. Opt.* **2019**, *58*, 1110–1120. [CrossRef]

41. Dawood, A.; Bashir, S.; Chishti, N.A.; Khan, M.A.; Hayat, A. Magnetic field effect on plasma parameters and surface modification of laser-irradiated Cu-alloy. *Laser Part. Beams* **2018**, *36*, 261–275. [CrossRef]

42. Lei, W. Temporal and Spatial Characteristics of Laser-Induced Plasma on Organic Materials and Quantitative Analysis of the Contained Inorganic Elements. Ph.D. Thesis, Université Claude Bernard-Lyon I; East China Normal University (Shanghai), Shanghai, China, 2012.

43. Rumsby, P.; Paul, J. Temperature and density of an expanding laser produced plasma. *Plasma Phys.* **1974**, *16*, 247–260. [CrossRef]

44. Akram, M.; Bashir, S.; Hayat, A.; Mahmood, K.; Ahmad, R.; Rahman, M.K. Effect of laser irradiance on the surface morphology and laser Induced plasma parameters of zinc. *Laser Part. Beams* **2014**, *32*, 119–128. [CrossRef]

45. Körner, C.; Mayerhofer, R.; Hartmann, M.; Bergmann, H.W. Physical and material aspects in using visible laser pulses of nanosecond duration for ablation. *J. Appl. Phys. A* **1996**, *63*, 123–131. [CrossRef]

46. Aristov, Y.I.; Tokarev, M.M.; Freni, A.; Glaznev, I.S.; Restuccia, G. Kinetics of water adsorption on silica Fuji Davison RD. *Micropor. Mesopor. Mat* **2006**, *96*, 65–71. [CrossRef]

47. Mansour, N.; Jamshidi-Ghaleh, K.; Ashkenasi, D. Formation of conical microstructures of silicon with picosecond laser pulses in air. *J. Laser Micro/Nanoeng.* **2006**, *1*, 10.2961. [CrossRef]

48. DeShazer, L.; Newnam, B.; Leung, K. Role of coating defects in laser-induced damage to dielectric thin films. *Appl. Phys. Lett.* **1973**, *23*, 607–609. [CrossRef]

49. Bashir, S.; Khurshid, S.; Akram, M.; Ali, N.; Ahmad, S.; Yousaf, D. Pulsed laser ablation of Ni in vacuum and N$_2$ atmosphere at various fluences. *Quant. Elec.* **2015**, *45*, 640–647. [CrossRef]

50. Sava, I.; Stoica, I.; Mihaila, I.; Pohoata, V.; Topala, I.; Stoian, G.; Lupu, N. Nanoscale analysis of laser-induced surface relief gratings on azo-copolyimide films before and after gold coating. *Polym. Test.* **2018**, *72*, 407–415. [CrossRef]

51. Tokarev, V. Viscous liquid expulsion in nanosecond UV laser ablation: From "clean" ablation to nanostructures. *Laser Phys.* **2006**, *16*, 1291–1307. [CrossRef]

52. Zehra, K.; Bashir, S.; Hassan, S.; Ahmed, Q.S.; Akram, M.; Hayat, A. The effect of nature and pressure of ambient environment on laser-induced breakdown spectroscopy and ablation mechanisms of Si. *Laser Part. Beams* **2017**, *35*, 492–504. [CrossRef]

53. Bleiner, D.; Bogaerts, A. Multiplicity and contiguity of ablation mechanisms in laser-assisted analytical micro-sampling. *Spectrochim. Acta B* **2006**, *61*, 421–432. [CrossRef]

54. Popok, V.; Prasalovich, S.; Samuelsson, M.; Campbell, E.E. Design and capabilities of a cluster implantation and deposition apparatus: First results on hillock formation under energetic cluster ion bombardment. *Rev. Sci. Instrum.* **2002**, *73*, 4283–4287. [CrossRef]

55. Ko, S.H.; Pan, H.; Hwang, D.J.; Chung, J.; Ryu, S.; Grigoropoulos, C.P.; Poulikakos, D. High resolution selective multilayer laser processing by nanosecond laser ablation of metal nanoparticle films. *J. Appl. Phys.* **2007**, *102*, 093102. [CrossRef]

56. Tarasenko, V.; Goncharenko, I.; Koval, N.; Orlovskii, V.; Fedenev, A.; Velikanov, S.; Borisov, V.; Podavalov, A.; Zolotov, M.; Podsezertsev, A. Study of the effect of infrared laser radiation on a steel surface. *Las. Phy.* **2003**, *13*, 1478–1486.

57. Lowdermilk, W.; Milam, D. Laser-induced surface and coating damage. *IEEE J. Quantum Electron.* **1981**, *17*, 1888–1903. [CrossRef]